ELSEVIER

Contents lists available at ScienceDirect

# Journal of Colloid And Interface Science

journal homepage: www.elsevier.com/locate/jcis



# Regular Article

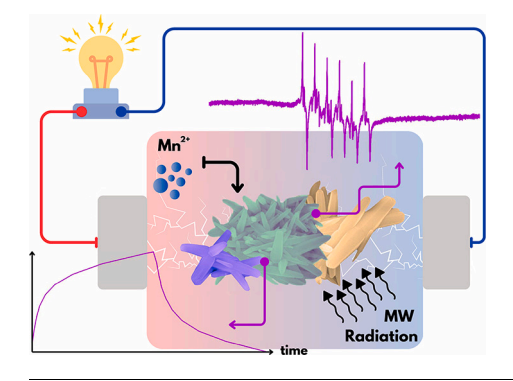


# 

Mohamad Hasan Aleinawi <sup>a, b</sup>, Ameen Uddin Ammar <sup>b, b</sup>, Duygu Şentürk <sup>a, b</sup>, Lucian Barbu-Tudoran <sup>c,b, b</sup>, Oluwatosin Johnson Ajala <sup>a, b</sup>, Defne Eşkin <sup>d, b</sup>, Feray Bakan Misirlioglu <sup>e, b</sup>, Arpad Mihai Rostas <sup>b, b</sup>,\*, Emre Erdem <sup>a,f, b</sup>,\*\*

- <sup>a</sup> Faculty of Engineering and Natural Sciences, Sabanci University, Tuzla, Istanbul, 34956, Turkey
- b National Institute for Research and Development of Isotopic and Molecular Technologies, Donat 67-103, Cluj-Napoca, 400293, Romania
- <sup>c</sup> Babes-Bolyai University, Kogalniceanu 1, Cluj-Napoca, 400347, Romania
- <sup>d</sup> Department of Chemistry, Faculty of Science, Ankara University, Beşevler, Ankara, 06100, Turkey
- e Nanotechnology Research and Application Center (SUNUM), Sabanci University, Tuzla, Istanbul, 34956, Turkey
- f Center of Excellence for Functional Surfaces and Interfaces (EFSUN), Sabanci University, Tuzla, Istanbul, 34956, Turkey

# GRAPHICAL ABSTRACT



# ARTICLE INFO

#### Keywords: ZnO Supercapacitors Defect engineering Microwave-assisted synthesis Mn<sup>2+</sup> doping

# ABSTRACT

Zinc oxide-based (ZnO) electrode materials have emerged as contenders for heightened cost efficiency, fast charge-discharge prowess, outstanding performance metrics, and remarkable cycle stability in supercapacitor technologies. Among the myriad synthesis techniques, the microwave-assisted approach distinguishes itself with an array of advantages, being time-efficient, eco-friendly, and adept at providing accurate control over the complex ZnO morphology. Introducing ions like Mn<sup>2+</sup> into the ZnO lattice further propels the electrochemical performance of supercapacitors into superior territories. Hence, this investigation meticulously prepared a series of undoped and Mn-doped ZnO materials utilizing a microwave-assisted synthesis method across four different microwave powers ranging from 160 to 800 W. Cutting-edge morpho-structural characterization techniques, including X-ray diffraction, scanning electron microscopy, electron paramagnetic resonance, photoluminescence, and Raman spectroscopy, were employed to delve into the structure and defect centers of the ZnO-based samples.

# https://doi.org/10.1016/j.jcis.2025.138012

Received 26 March 2025; Received in revised form 21 May 2025; Accepted 26 May 2025 Available online 30 May 2025

<sup>☆</sup> Supplementary Information File available.

<sup>\*</sup> Corresponding author.

<sup>\*\*</sup> Corresponding author at: Faculty of Engineering and Natural Sciences, Sabanci University, Tuzla, Istanbul, 34956, Turkey. *E-mail addresses*: arpad.rostas@itim-cj.ro (A.M. Rostas), emre.erdem@sabanciuniv.edu (E. Erdem).

It has been conclusively demonstrated that the concentration of  $\mathrm{Mn^{2+}}$  is pivotal, offering additional charge carriers without compromising the crystallinity of ZnO while also enhancing diffusion correlated with Faradaic redox reactions—thereby escalating the supercapacitor's properties. A doping concentration of 2% Mn-ions balances charge carriers with structural integrity. This sample achieved a specific capacitance of 340 F/g, a power density of 59.7 kW/kg, and an energy density of 47.1 Wh/kg. Across the board, all samples demonstrate impressive stability, retaining over 70% capacity after 5000 charge-discharge cycles. Notably, ZnO with 2% Mn synthesized at 160 W excels with over 90% capacitance retention. This distinct behavior is attributed to the transformative influence of Mn ion doping on ZnO's structural and morphological attributes.

#### 1. Introduction

The growing demand for energy and environmental contamination has accelerated the development of energy storage and conversion technologies. Among these technologies, supercapacitors have been extensively researched and utilized in various domains, including backup power systems, hybrid electric vehicles, military high-power equipment, and rail transportation. A supercapacitor is a high-capacity energy storage device with elevated power density, prolonged cyclic stability, and fast charging and discharging efficiency. The power density of supercapacitors is approximately one thousand times greater than that of rechargeable batteries [1,2]. Supercapacitors significantly depend on electrode materials, which play a crucial role in influencing their overall performance. Transition metal-based electrode materials have been extensively studied to achieve cost-effectiveness, rapid charge-discharge capabilities, superior performance, and extended cycle longevity for supercapacitors [3]. Transition metal oxides (TMOs), including ZnO [4], MnO<sub>2</sub> [5], and RuO<sub>2</sub> [6], have been thoroughly investigated for supercapacitor applications due to their high capacitance and electrochemical stability. However, the primary challenges for transition metal oxide electrode materials are still limited by low energy density, increased internal resistance at material interfaces, insufficient mechanical durability, and pressing environmental concerns. Recent research has demonstrated a significant enhancement in the performance of transition metal-based oxides [7-9].

ZnO is a promising material, significant for its essential attributes, including a wide band gap (3.44 eV) [10,11], considerable exciton binding energy (60 meV), low power threshold for optical pumping [12], efficient ultraviolet (UV) emission [13], high piezoelectric coefficient (d33 = 9.093 pm/V, which increases to 26.7 pm/V in the nano regime) [14], and favorable pyroelectric coefficient, all while remaining nontoxic [15]. These features enable various applications in devices related to short-wavelength optoelectronic communications [16], photovoltaics [17], sensors and transducers [18], supercapacitors [19, 20], UV emitters [21], photodetectors [22], and gas or biosensors [23].

ZnO based nanomaterials have various types of methods to synthesize it [24], for instance, chemical methods (sol-gel, hydrothermal and solvothermal, precipitation, chemical vapor deposition, microemulsion, and microwave methods), physical methods (laser ablation, ball milling, and thermal evaporation methods) and biological methods (green and enzymatic synthesis methods).

The most prominent methods to synthesize ZnO nanomaterials [25] are co-precipitation [26–28], sol-gel [29–31], ball-milling [32–34], hydrothermal [35,36], solvothermal [37–39], and microwave [40–42] techniques. The synthesis method affects its shape, size, and spatial structure [25]. Because of their differences in structure, they have different applications. The microwave synthesis method has many applications and stands out for several properties. For instance, microwave-assisted synthesis is a rapid method that can synthesize ZnO in a few minutes. It is environmentally friendly as it requires fewer chemicals and less energy [43], and it allows precise control over the morphology of the ZnO NMs by varying the reaction time, microwave power, and precursor concentration [43–45]. Several studies have found that ZnO composite materials exhibit high energy density, high specific

capacitance [46], and long cycle life of about 1000 [47]. This indicates that these composites are suitable for energy storage applications

Moreover, as evidenced in many studies, another key factor that affects the supercapacitor's property and performance is the defect centers present in the materials [48-50]. A defect center is an imperfection that disrupts the periodic arrangement of atoms in a crystal lattice or molecular structure. These defects can significantly influence materials' physical, chemical, and electronic properties, affecting their performance in technological applications like supercapacitors. These defects, which include vacancies, edge defects, and other structural irregularities, can modulate the surface microstructure and electrochemical properties [51]. Defects can increase the specific capacitance of supercapacitors by providing extra space for charge storage [52], improving electronic properties and ionic transport [53]. Experiments and theoretical calculations have proven that the electronic structures are related to oxygen vacancies that serve as shallow donors to improve the carrier concentrations and enhance the electrical conductivity to boost the reaction kinetics [54]. Besides affecting the electronic structures and electrical conductivity, the interlayer spacing can be expanded by introducing oxygen vacancies, which boost faster charge storage kinetics and enhance the redox reactions for improved electrochemical performances [19]. Doping can also help improve the electrochemical performance of the SCs and modulate the electronic structure by tuning the band gap, improving conductivity. Dopants can create more defects in the crystal lattice, enhancing the electrochemical performance, and some dopants can create redox activity in the supercapacitor, enhancing the pseudocapacitance phenomenon [55].

Furthermore, surface defects can improve electrochemical performance by reducing the charge transfer resistance [56]. Materials' storage capacity can be increased synergistically through enhanced ion adsorption, reduced ion transport resistance, and facilitated ion migration by combining intrinsic defects and functional groups [57]. Several techniques are used to characterize defect centers present in materials, such as photoluminescence (PL), Raman, and Electron Paramagnetic Resonance (EPR) spectroscopy.

Photoluminescence investigations demonstrate divergent emission characteristics in bulk and nanostructured ZnO [58]. In bulk ZnO, nearband-edge (NBE) emissions dominate, which are associated with direct bandgap recombination processes. Whereas defect-related deep-level emissions (DLE) arise from oxygen vacancies ( $V_{\rm O}$ ), zinc interstitials ( $Zn_{\rm I}$ ), and extrinsic defects. Incorporating Mn in nanostructured ZnO:Mn reduces the photoluminescence signal, as extrinsic Mn shortcomings replace intrinsic ZnO defects [59,60]. This phenomenon indicates that Mn incorporation contends with intrinsic flaws, resulting in non-radiative recombination pathways and diminished excitonic emission. Furthermore, nanostructure size constriction amplifies surface states, diminishing brightness relative to bulk ZnO [4].

Raman spectroscopy is crucial for examining phonon interactions, oxygen vacancies, and oxidation states in ZnO:Mn. Raman graphs of ZnO display distinct Raman-active vibrational modes, including  $E_2$ (high) (437 cm $^{-1}$ ) and  $A_1$ (LO) (570 cm $^{-1}$ ), with the latter being especially responsive to oxygen vacancy defects [61]. The introduction of Mn modifies these vibrational modes, influencing local symmetry and charge distribution. An escalation in defect-related modes signifies

a greater density of oxygen vacancies, pivotal in changing the electrical and optical characteristics of ZnO:Mn. Moreover, the oxidation states of Mn  $(Mn^{2+}, Mn^{3+})$  affect the extent of lattice deformation, hence influencing phonon confinement and electron-phonon interactions [62].

EPR is an efficient technique for investigating the local electronic surroundings of paramagnetic dopants in a host lattice. For example, the EPR spectrum of Mn ions used to dope ZnO can give important information about the structure of the host material [63]. The core-shell model effectively examines hyperfine interactions by differentiating between Mn ions present in the core of ZnO nanoparticles and those positioned on the surface (shell) regions [64,65]. Doping Mn ions maintains intrinsic ZnO-like symmetry, but the surface Mn ions undergo local strain, modified coordination, and defect-induced disturbances. These modifications affect the g-values, hyperfine splitting, higher-order spin parameters such as zero-field splitting, and relaxation dynamics, essential for customizing the magnetic and electrical properties of ZnO:Mn [66,67,63].

Although ZnO is a promising material for supercapacitor electrodes due to its high theoretical capacitance and natural abundance, it displays very low electrical conductivity, limiting efficient electron movement within the electrode [68]. ZnO electrodes may undergo structural changes, such as volumetric expansion and contraction, after successive charge/discharge cycles, leading to mechanical stress and deterioration [69]. Manganese (Mn) doping has been investigated to enhance the electrochemical performance of zinc oxide in supercapacitor applications [70,4,71]. Research suggests that incorporating Mn into ZnO can improve electrical conductivity, increase specific capacitance, and enhance cyclic stability [70]. Studies show that Mn-doped ZnO electrodes exhibit superior specific capacitance and better cyclic stability than undoped ZnO electrodes [4]. Furthermore, Mn doping can create redox-active sites, enhancing pseudo-capacitance and total energy storage capacity [72]. The results imply that Mn-doped ZnO represents a viable material for high-performance supercapacitors.

Aleinawi et al. [73] examined the substantial impact of varying microwave power during the hydrothermal synthesis of Mn-doped ZnO, and the microwave-assisted technique produced uniform Mn:ZnO rods on a micrometer scale, noting that increased microwave power levels expedite nucleation and crystal development, leading to larger, well-crystallized ZnO particles with fewer defects. Excessive microwave power may lead to particle aggregation, reducing the active surface area. Lower microwave power levels generate smaller particles with increased porosity, facilitating enhanced ion diffusion. However, inadequate energy may result in incomplete Mn incorporation into the ZnO lattice. Manganese-doped ZnO has emerged as a highly promising electrode material for supercapacitors due to the unique synergy between the semiconducting behavior of ZnO and the rich redox potential of Mn ions. On its own, ZnO can show limited electrochemical activity, primarily low conductivity and the absence of pseudocapacitance for charge storage. However, when doped with Mn ions, the material undergoes significant structural and electronic transformations that enhance its performance in supercapacitor systems [4]. One of the most notable effects of Mn doping is improved electrical conductivity. The substitution of  $\mathrm{Zn}^{2+}$  ions with  $\mathrm{Mn}^{2+}$  or  $\mathrm{Mn}^{3+}$  introduces localized states in the band structure of ZnO. These states facilitate charge transfer and reduce the bandgap, allowing electrons to move more freely through the electrode material. This enhanced conductivity is crucial for faster charge-discharge cycles and better overall rate capability. In addition to conductivity improvements, manganese ions contribute active redox centers that enable pseudocapacitive behavior. Unlike pure ZnO, which primarily stores charge through electrostatic accumulation at the surface (electric double-layer capacitance), Mn-doped ZnO participates in faradaic reactions. These redox processes, particularly involving the Mn<sup>2+</sup>/Mn<sup>3+</sup> and Mn<sup>3+</sup>/Mn<sup>4+</sup> transitions, allow the material to store additional charge within its bulk, significantly increasing the specific capacitance [57,74].

In addition to its beneficial magnetic and electrical properties, Mn enhances ZnO's atomic alignment. Pearton et al. [75], Zheng et al. [76] showed that a small amount of Mn doping greatly enhances the atomic alignment and grain formation, which increases electrochemical activity. Specifically, the ionic radius of  $\mathrm{Mn^{2+}}$  (0.66 Å) closely matches that of  $\mathrm{Zn^{2+}}$  (0.60 Å), facilitating the substitutional doping process. This similarity in ionic radii minimizes structural incompatibilities, resulting in controlled lattice distortion and substitutional defects that further improve the material's functional properties [77].

Numerous studies have explored Mn-doped ZnO using conventional hydrothermal synthesis; however, the effects of varying microwave power during this process have not been thoroughly investigated. The novelty of our study lies in the integrated approach combining binderfree, all-in-one supercapacitor device fabrication with a systematic investigation of defect engineering via microwave-assisted synthesis and Mn doping. Unlike conventional methods that rely on carbon additives and binders, which often obscure the intrinsic electrochemical behavior of the active material, we employed a custom-designed twopoint mounting device to assemble supercapacitors directly from the synthesized ZnO materials. This approach allows for a more accurate assessment of the electrochemical performance of the active material itself. Moreover, we controlled the Mn<sup>2+</sup> concentration, monitored its substitutional incorporation and oxidation state using detailed EPR spectroscopy analysis, which provided insights into the interaction between intrinsic (e.g., Zn vacancies) and extrinsic (dopant-related) defect centers. The combined use of EPR, PL, Raman, and structural analysis allowed us to correlate these defect characteristics with the observed variations in electrochemical behavior.

Additionally, the novelty extends to the tunability of morphology and defect profiles by varying the microwave power, offering a simple yet powerful route to tailor size, aspect ratio, and crystallinity of ZnO nanostructures. This defect-sensitive synthesis-structure-performance correlation is not extensively explored in the literature, especially for Mn-doped ZnO synthesized under varying microwave conditions. Therefore, the study provides new insights into how dopant concentration and synthesis energy input synergistically affect defect chemistry and electrochemical properties.

#### 2. Materials and methods

## 2.1. Synthezis method

As described in our previous work, we synthesized undoped and Mn-doped ZnO via a microwave-assisted synthesis route [73] (Fig. 1). The synthesis was carried out using zinc nitrate hexahydrate (ZNH - $Zn(NO_3)_2 \cdot 6H_2O$ , Acros Organics, 98% purity, CAS No.: 10196-18-6), hexamethylenetetramine (HMTA - (CH<sub>2</sub>)<sub>6</sub>N<sub>4</sub>, Merck, 99% purity, CAS No.: 100-97-0), the source of Mn was manganese acetate tetrahydrate (MAT - (CH<sub>3</sub>COO)<sub>2</sub>Mn·4H<sub>2</sub>O, Acros Organics, 99% purity, CAS No.: 6156-78-1), and methanol (CH3OH, Sigma Aldrich, 99.8% purity, Cas No.: 67-56-1) as solvent. A solution of 25 mM of ZNH and MTA was prepared by dissolving the precursors in deionized (DI) water and magnetically stirring for 1 hour at 600 rpm to ensure dissolving of the precursors. The solution was then inserted in a conventional microwave oven, and the synthesis was carried out at different microwave powers of 160, 320, 640, and 800 W. The obtained powders were then filtered using filtration papers, washed thoroughly with DI water and alcohol, and left to dry out in an oven at 80 °C overnight. Mn-doped ZnO was synthesized by following the same steps aforementioned, with the addition of MAT dissolved in methanol to the ZNH and MTA solution, and to ensure sufficient energy for the incorporation of Mn ions into the structure of ZnO, the powder was subjected to an additional heat treatment process at the end of the synthesis. The powder was heated to 400 °C for 4 h and cooled to room temperature afterward.

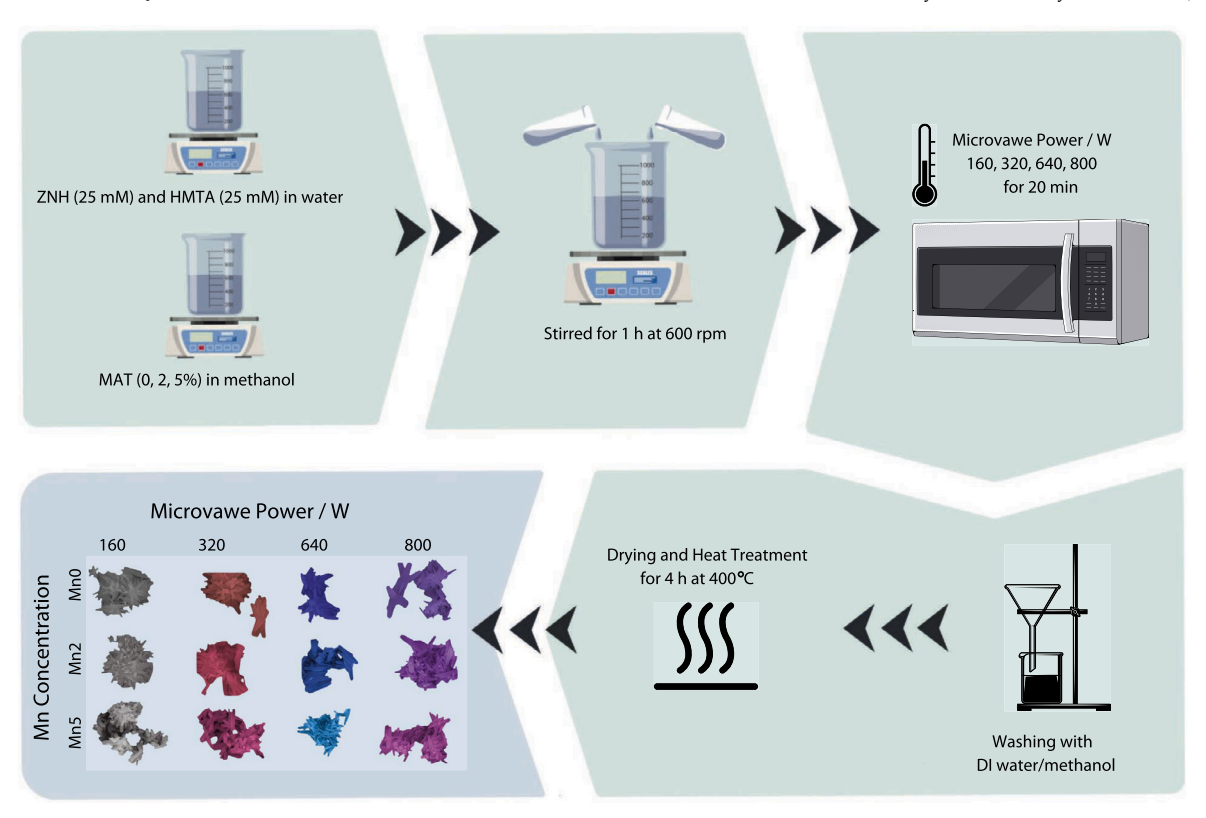


Fig. 1. Schematic representation of the microwave-assisted hydrothermal technique used to synthesize ZnO and Mn-doped ZnO nanorods.

#### 2.2. Morpho-structural characterization methods

For morphological assessment using scanning electron microscopy (SEM), the samples were sputter-coated with 7 nm of gold in a Polaron E–5100 plasma-magnetron sputter coater (Polaron Equipment Ltd., Watford, UK) in the presence of argon (45 s at 2 kV and 20 mA). Ultrastructural images were obtained using a Hitachi SU8320 CFEG scanning electron microscope (Hitachi, Chiyoda, Japan) at 30 kV and different magnification powers. Energy-dispersive X-ray spectroscopy (EDX) was used to perform semi-quantitative elemental analysis using an EDX detector X-mas 80 (Oxford Instruments, Abingdon, UK).

The specific surface area analysis was carried out using  $\rm N_2$  adsorption-desorption isotherms using a Micromeritics 3Flex surface characterization analyzer (Micromeritics Instrument Corp., Norcross, GA, USA). Before analysis, the samples were degassed under vacuum at 200 °C for 12 h to remove adsorbed gases and moisture, and the measurements were conducted at 77 K using high-purity nitrogen gas as the adsorbate. The Brunauer-Emmett-Teller (BET) method was applied to calculate the specific surface area from the linear region of the adsorption isotherm (typically at relative pressures  $P/P_0$  between 0.05 and 0.30).

The crystalline structure of the samples was evaluated by taking the X-ray diffraction (**XRD**) patterns using a Bruker D2 phase diffractometer in the  $2\theta$  range of 10 to 90° with a step size of 0.02°.

The defect structure of ZnO and the presence of paramagnetic Mn ions were investigated by photoluminescence (PL), Raman, and electron paramagnetic resonance (EPR) spectroscopy. PL spectra were measured using an FS5 spectrofluorometer (Edinburgh Instruments) equipped with a 150 W CW Ozone-free Xenon arc lamp, a Czerny–Turner with plane grating monochromators, and a PMT-900 emission detector. The Raman spectra were acquired using an InVia Raman spectrometer (Renishaw, UK) with an upright microscope and a 532 nm frequency-doubled Nd:YAG solid-state laser. The laser power was set to 1% to minimize sample degradation during data acquisition. EPR spectroscopy measurements were performed on a Bruker E500 ELEXSYS spectrometer at Q-band (33.9 GHz) under identical conditions.

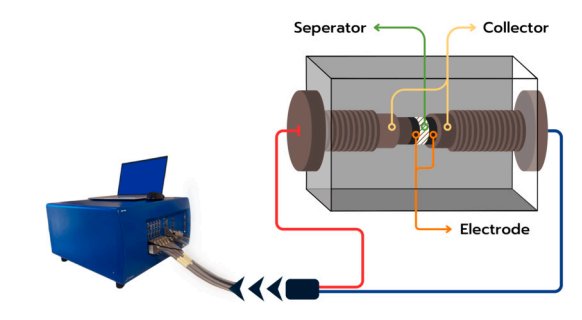


**Fig. 2.** Schematic of the double electrode symmetric supercapacitor configuration used to measure the supercapacitive properties of the ZnO-based materials.

# 2.3. Electrochemical properties measurements

Supercapacitor devices (SC) with a double electrode configuration were assembled, as shown in Fig. 2, to asses the supercapacitive properties of the ZnO-based materials. The double electrode configuration was used to study the synergy between the electrode materials and between the electrode and electrolyte. To accurately analyze the electrodes, symmetric SC devices have been used for all materials. The electrode material was mixed with Polyvinylidene Fluoride (PVDF) as a binder and dissolved in a 6 M Potassium Hydroxide (KOH) solution. To ensure a homogeneous slurry, the mixture was dissolved in a sonicator at 70 °C. The slurry was coated on top of two electrodes and left to dry on a hot plate at 90 °C. Finally, the electrodes were separated with a glass fiber separator and wetted with a few drops of 6 M KOH, which was used as the electrolyte. The total mass of the electrode material used in the study is 25 mg, coated on top of a circular-shaped stainless steel bolt with a radius of 1.25, yielding a mass loading of 2.5 mg/cm<sup>2</sup>. This mass loading was chosen to maintain consistency with the literature while ensuring robust electrochemical performance. The SC devices were then connected to a Biologic VMP300 multichannel potentiostat. Several different methodologies were used for the analysis,

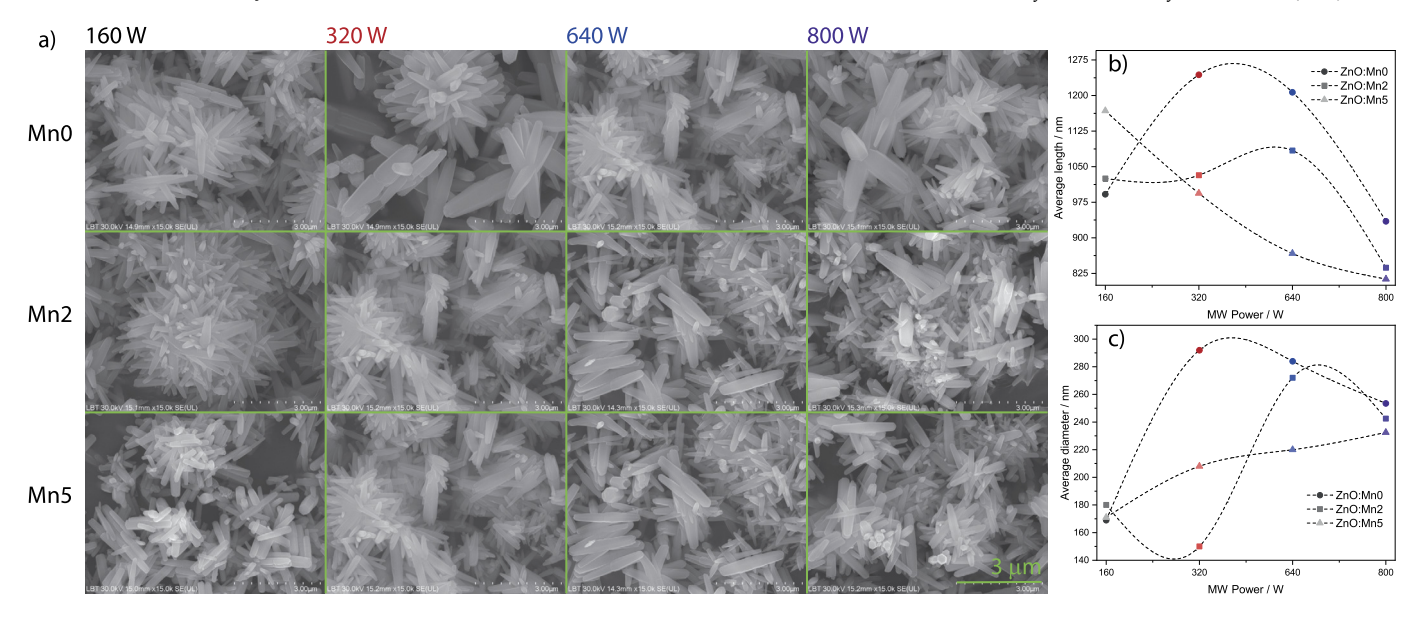


Fig. 3. SEM micrographs of the undoped and Mn-doped ZnO materials synthesized at different microwave powers showing the nanorod-shaped structures (a) and the average nanorod length (b), and diameter (c) obtained from the histograms of the SEM images.

such as cyclic voltammetry (CV) that involves subjecting the working electrodes to a linearly changing voltage, to study the redox behavior, the specific capacitance of the SC devices, and the electrochemical stability. Electrochemical impedance spectroscopy (PEIS) under potentiostatic conditions, voltage holding test (VH), and galvanostatic cycling with potential limitation (GCPL).

#### 3. Results and discussion

The undoped and Mn-doped samples synthesized at various microwave powers were first thoroughly characterized by evaluating the impact of the dopant ions and the microwave power on their morphology and structure. The samples' morphology was assessed by studying the SEM micrographs shown in Fig. 3 (a) and S-SEM\*. At a lower microwave power of 160 W for ZnO:MnO samples, the formations show reduced size and an almost homogeneous morphology. Increasing the power to 340 W yields significant elongation and an increase in diameter. Increasing power to 640 W further enhances consistency and size. At maximum power (800 W), the structures commence degradation, displaying breakage and uneven shapes. The ZnO:Mn2 samples @ 160 W exhibit more clustering and density than undoped ZnO. Raising the microwave power to 340 W and 640 W demonstrates a progressive increase accompanied by enhanced density. At 800 W, the structures exhibit relatively low deformation relative to the lower power samples. ZnO:Mn5 @ 160 W displays a closely aggregated structure, and its growth is suppressed relative to the undoped sample. As the microwave power increases, the morphology becomes progressively uneven, indicating that excessive doping may disrupt the growth process. The 800 W sample exhibits significant aggregation with diminished aspect ratios, suggesting over-doping or microwave-induced deterioration. The length and diameter of the ZnO rods were estimated from the SEM micrographs (see Fig. S-SEM\*). The average diameter of ZnO:Mn0 reaches its maximum at approximately 340 W, which suggests that this power level is optimal for growth. As the concentration of Mn increases, the peak diameter shifts to higher power levels, specifically at 640 W. This indicates a relationship between growth efficiency and microwave power. Additionally, increasing Mn doping to 5% reduces diameters, implying that the presence of Mn ions contributes to a structural reduction. To further emphasize the effect of the morphology change, ImageJ software was used to obtain the average nanorod length and diameter from the histograms of individual nanorods as shown in Fig. S-SEM\*, and the results are summarized in Fig. 3 (b) and (c). The results show a tendency to maximize nanorods' length and minimize diameter at lower microwave powers, thus maximizing the aspect ratio (AR) of the nanorods at lower microwave powers. However, the density of the nanorods is minimized at said lower microwave powers.

BET measurements have been applied to evaluate the surface area on the materials' capacitive performance. BET technique provides a reliable estimation of the specific surface area by analyzing nitrogen adsorption-desorption isotherms, offering insight into the accessible active sites available for charge storage. Thus, BET is crucial for understanding and optimizing the electrode materials' structure–performance relationship in supercapacitor applications. BET results are summarized in Figs. 4 (a) and S-BET\*, showing the N<sub>2</sub> adsorption-desorption isotherms, and the linear BET equation, respectively. The BET equation is expressed as  $\frac{1}{V\left(\frac{P_0}{P_0}-1\right)} = \frac{C-1}{V_mC} \cdot \frac{P}{P_0} + \frac{1}{V_mC}.$  Where V is the volume of the gas adsorbed,

 $V_m$  is the adsorbed monolayer, P is the adsorbate gas' monolayer equilibrium pressure,  $P_0$  is the adsorbate gas' saturation pressure, and C is the BET constant. The BET surface area is obtained from the linear region between 0.05 to 0.3 using the slope and the intercept. ZnO:Mn2 @ 160 W shows the highest specific surface area of 61  $\mbox{m}^2/\mbox{g}$ , a value that decreases as the microwave power used in the synthesis increases, indicating that high microwave powers reduce the specific surface area of ZnO. These results agree with the results obtained from the SEM histograms. While 61 m<sup>2</sup>/g is not necessarily a high value, it is within the expected range for Mn-doped ZnO nanowires, which is also affected by the morphology of ZnO and the dopant concentration [78,79]. Despite the low specific surface area of Mn-doped ZnO nanowires, the material can still display efficient electrochemical performance due to the fast pathway of electrons favored by the direct and aligned structure of the nanowires. In addition to that, having a high aspect ratio offers sufficient surface exposure to electrolyte ions, facilitating active ion adsorption and redox reactions, especially along the nanowires' sidewalls [80,81]. The aforementioned properties become especially efficient when the dominating working mechanism in the supercapacitor devices is the diffusive mechanism, which involves Faradaic redox reactions, as will be discussed in the Dunn technique section.

X-ray diffraction is a powerful and widely used analytical technique for characterizing crystalline materials. The results of XRD analysis are shown in Figs. SI-XRD\* and 4(b). The hexagonal wurtzite structure (P6 $_3$ mc) is ZnO's most stable crystalline structure [82]. All samples show the typical peaks associated with this structure at miller indices of (100), (002), (101), (102), (110), (103), (112), and (201) correspond-

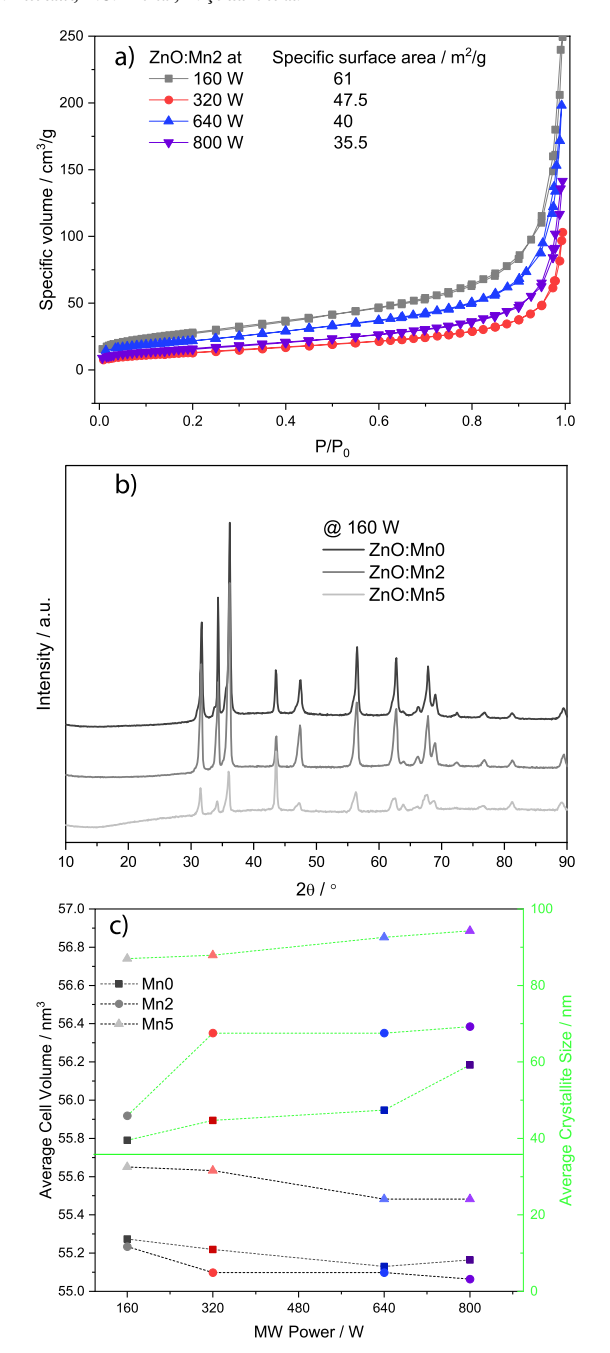


**Fig. 4.**  $N_2$  adsorption-desorption isotherms of the 2% Mn-doped ZnO nanorods synthesized at different microwave powers (a), XRD diffractograms of the undoped and Mn-doped ZnO materials synthesized at 160 W microwave power (b) and the average crystallite size and average cell volume as a function of the microwave power (c).

ing to  $2\theta$  angles of 31.77, 34.42, 36.25, 47.54, 56.60, 62.86, 67.96, and 69.10° respectively, obtained from the ICDD (JCPDS card no. 36-1451). Furthermore, an additional peak can be observed at around  $2\theta$  43.5°, which is not characteristic of the wurtzite structure. The fact that this peak can be observed even in ZnO:MnO samples implies that this peak is most likely associated with ZnO-related impurities such as elemental Zn or Zn(OH)<sub>2</sub> [83–85]. The intensity of the peak mentioned above seems to decrease with increasing microwave power during synthesis due to the higher probability of converting Zn(OH)<sub>2</sub> into ZnO as reported elsewhere [86]. Rietveld refinement has been applied to the XRD results to obtain the average crystallite size and average cell volume as shown in Figs. S-XRD\* and 4(c). The refinement results are summarized in Ta-

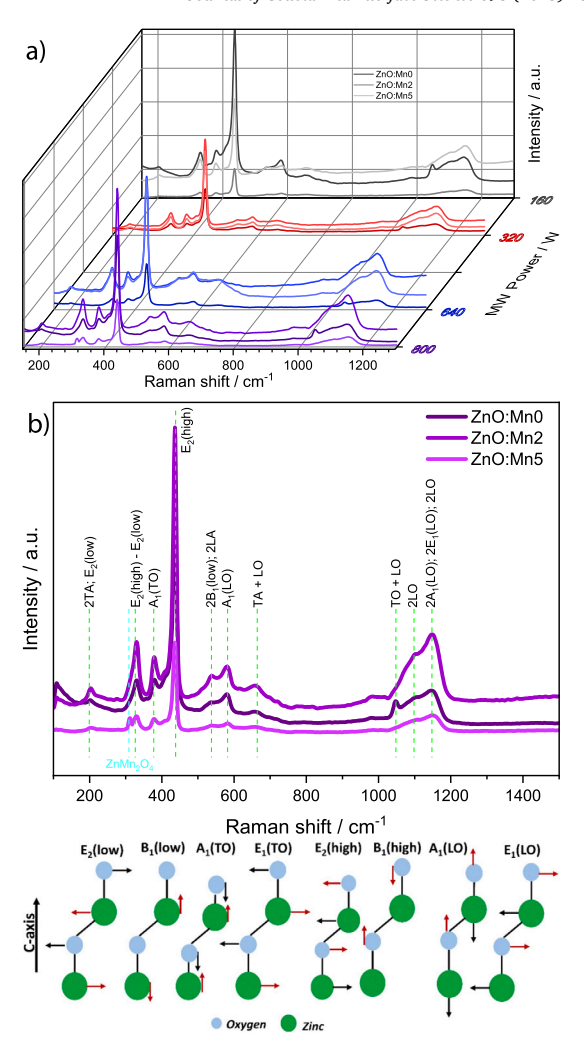


**Fig. 5.** The first-order and second-order Raman spectra of undoped and Mndoped ZnO samples synthesized at different microwave powers (a) and a comparison between the Raman spectra of the undoped and Mn-doped ZnO synthesized at a microwave power of 800 W, where all the observable Raman modes are indicated together with all possible Raman modes that are ZnO specific.

ble T-XRD\*. The Mn dopant seems to slightly alter the lattice values of ZnO, which implies a successful integration of the Mn ions into the ZnO structure. In addition, the average crystallite size increases with increasing Mn dopant concentration and increases with the microwave power during synthesis, implying favored crystal growth conditions at higher microwave powers. However, this should not be interpreted as a straightforward improvement in crystallinity. The broadening of XRD peaks with increasing Mn content reflects the introduction of lattice strain and microstructural disorder, particularly at intermediate doping levels. These strain effects may originate from ionic radius mismatch. The average cell volume, on the other hand, behaves differently, as it decreases with increasing microwave power and by integrating Mn ions into the structure of ZnO for the ZnO:Mn2 samples. Furthermore, the cell volume increases again for ZnO:Mn5 samples, indicating a possible solubility limit. Mn has an ionic radius of 0.66 Å, while Zn has an ionic radius of 0.6 Å. Thus, an increase in the cell volume shall be expected after the incorporation of Mn into the ZnO lattice, as observed in the ZnO:Mn5 samples. However, due to the microstructural strain effects occurring at lower concentrations of Mn in the ZnO:Mn2 samples, we observe a small reduction in the cell volume, and the effect of this microstructural strain increases with increasing microwave power [87,88].

Raman spectroscopy provided a detailed molecular-level understanding of the lattice dynamics in the synthesized ZnO nanostructures. The spectra depicted in Fig. 5(a) and S-Raman\* validate the successful synthesis of undoped and Mn-doped ZnO using various microwave powers during the synthesis procedure. In standard backscattering experiments, ZnO exhibits a dominant presence of E<sub>2</sub> modes, which act as a unique Raman signature [89–91]. In the hexagonal wurtzite (P63mc) ZnO structure, the phonon count is determined by the number of atoms within the unit cell, resulting in 12 phonon modes, including three acoustic ones [89]. In Fig. 5 (b), a distinct Raman peak observed at approximately 436  $\,\mathrm{cm^{-1}}$  corresponds to the  $\mathrm{E_2}(\mathrm{high})$  mode, which serves as a key spectral marker of the wurtzite ZnO phase [49]. The E<sub>2</sub>(low) mode was not detected; however, a vibrational feature near 330 cm<sup>-1</sup> is commonly associated with a second-order Raman process and is attributed to the  $E_2$ (high) -  $E_2$ (low) difference mode [49]. Additionally, the inherent polarity of the wurtzite crystal structure causes the A<sub>1</sub> and E<sub>1</sub> phonon modes to split, leading to the formation of transverse optical (TO) and longitudinal optical (LO) phonons. The A<sub>1</sub>(TO) mode was observed at 379 cm<sup>-1</sup>, while A<sub>1</sub>LO) mode was observed near 580 cm<sup>-1</sup>, which becomes prominent when the c-axis of the wurtzite ZnO is oriented parallel to the sample surface. In the high-frequency region, distinct second-order features emerge, attributed to LO overtones and combinations of LO modes. A weak shoulder around 1105 cm<sup>-1</sup> is likely associated with 2LO scattering from flat bands along the A-L-M line [89-91,49]. This peak may also result from the superposition of  $2A_1(LO)$  and  $2E_1(LO)$  modes at the  $\Gamma$  symmetry point of the Brillouin zone. The two-phonon difference modes fall within the frequency range of the one-phonon branches. In contrast, two-phonon sum modes and higher-order multi-phonon processes primarily govern frequencies above  $580 \text{ cm}^{-1}$ .

Raman spectroscopy investigation of Mn-doped ZnO structures reveals significant modifications in the vibrational properties due to Mn incorporation. Doping can induce peak shifts, broadening, and intensity variations in the characteristic ZnO modes. Additional Raman modes may appear, associated with local vibrational modes of Mn-related defects, disorder-induced activation of normally silent modes, and possible secondary phases like ZnMn<sub>2</sub>O<sub>4</sub> [92]. As shown in Fig. 5(b), for the synthesis performed at 800 W, the weak band at 310 cm<sup>-1</sup> corresponds to the octahedral (BO<sub>6</sub>) site of ZnMn<sub>2</sub>O<sub>4</sub> [49]. Another band, typically observed around 670 cm<sup>-1</sup> and associated with oxygen motion in the tetrahedral AO<sub>4</sub> group with A<sub>1</sub>g symmetry, is not visible in this case due to its overlap with the TO + LO mode. The TO + LO second-order Raman mode is absent at both Mn doping concentrations, as shown in Fig. 5(a). This disappearance is likely due to defects introduced by Mn incorporation, such as oxygen vacancies or Zn/Mn interstitials, which alter phonon dispersion and suppress specific vibrational modes. Defectinduced scattering can weaken or eliminate certain phonon interactions, leading to the observed suppression of this mode.

Photoluminescence spectroscopy is a useful characterization technique to explain defect-related emissions and how doping can impact emissions from intrinsic defect centers. Fig. 6(a) shows the PL spectra of the undoped and Mn-doped ZnO synthesized at 160 W. Fig. S-PL\* shows the remaining PL spectra of all other samples synthesized at different microwave powers. The Gaussian deconvolution fit was applied to all the PL spectra, with the results presented in Fig. S-PLfit\* of all the samples. At the same time, Fig. 6(b) shows the deconvolution of ZnO:Mn2, the best-performing sample regarding energy storage properties, as presented in the following. In Fig. 6(a), all samples show two major peaks, one with a smaller intensity centered around 415 nm, and the second peak broader and more intense centered around 590 nm for undoped ZnO. In contrast, we observed a shift in the red region for the doped sample for this peak, which is now centered around 640 nm. We observed a significant change in intensity and peak position in the doped samples compared with the undoped ZnO. Suppressing the PL intensity for the doped samples showed successful incorporation of Mn ions in the ZnO lattice. This led to extrinsic defect centers dominating

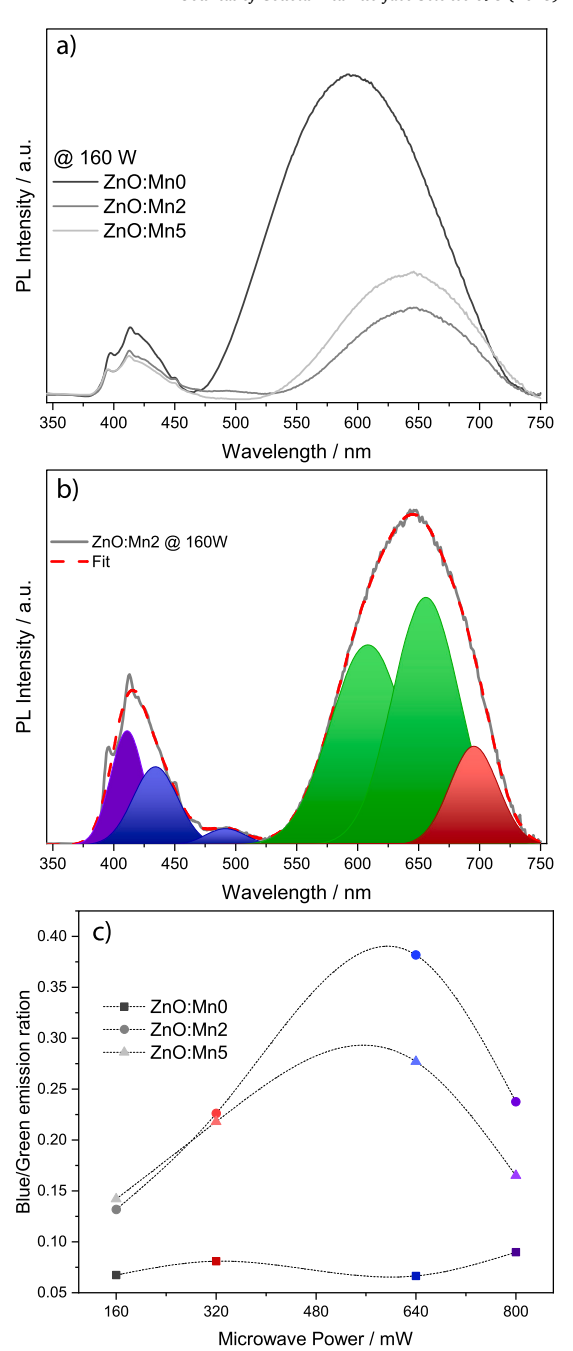


**Fig. 6.** PL emission spectra of undoped and Mn-doped ZnO samples synthesized at 160 W microwave power (a), and the deconvolution of the peaks of ZnO:Mn2 @ 160 W showing the different emission maxima at different wavelength (b), as well as the Blue-to-Green emission ratios of all samples (c).

the intrinsic ones as reported previously [93,70]. In Fig. 6(b), the violet emission centered around 390 nm with small intensity is associated with the near band gap emission (NBE), the blue emission is associated with zinc vacancies, while the green and red emissions are associated with the transition from Zinc interstitial to oxygen vacancy ( $V_O$ ) (oxygen vacancy complexes) and oxygen interstitial ( $O_i$ ) respectively [94,73]. The deconvolution in Figs. 6(b) and S-PLfit\* shows that with Mn doping, the intensity of zinc vacancy-related emissions is reduced, highlighting that Mn ions replace the zinc vacancies ( $V_{Zn}$ ). The dopant Mn ions also occupy interstitial positions, changing the  $V_O$  defect environment. This is highlighted by the reduction in green and red emissions with a prominent redshift for the doped sample. Fig. 6(c) shows the blue/green emission ratio of all samples. The reduction of intensities is visible for all

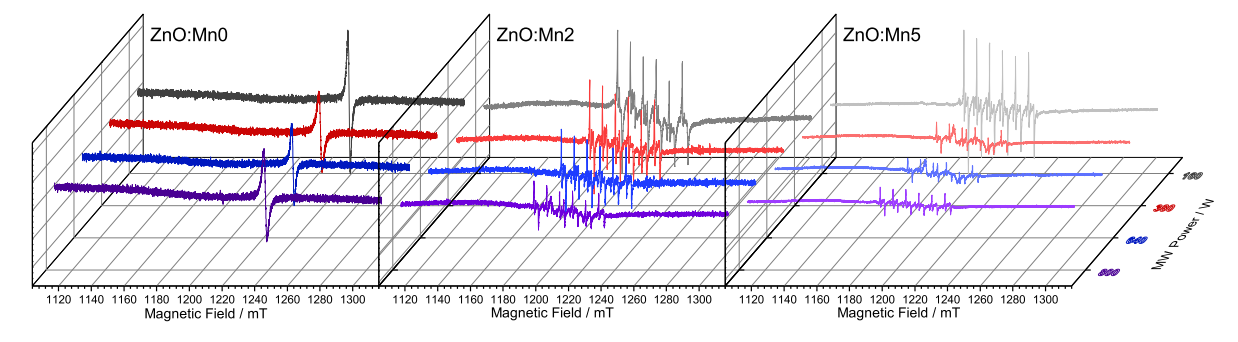


Fig. 7. Q-band EPR spectra of ZnO:Mn0, ZnO:Mn2, and ZnO:Mn5 samples synthesized at different microwave powers. The undoped samples present a resonant line at  $g \approx 1.96$ , attributed to intrinsic defects like Zn vacancies, while the Mn-doped ZnO samples display typical anisotropic sextet hyperfine lines of Mn<sup>2+</sup> centers.

the doped samples at each microwave power, hinting at the successful incorporation of Mn ions in the ZnO lattice at each microwave power.

Fig. 7 and S-EPR\* illustrate the Q-band EPR spectra for both undoped and Mn-doped ZnO. In the undoped samples, a resonant line appears around g  $\approx 1.96$ , attributed to intrinsic defects like Zn vacancies [95]. The intensity of this resonant line varies depending on the microwave power utilized during the material's synthesis. This variation is linked to changes in ZnO size, as described by Erdem [66]. The core-shell model employed here elucidates the emergence and disappearance of the EPR signals, suggesting that the signal at g  $\approx 1.96$  arises from core (bulk) defects. Comparative analyses across different sample sizes using both EPR and PL [14,96], together with existing theoretical works [97,98], confirm that the resonance at 1.96 relates to negatively charged Zn vacancies ( $V_{\rm Zn}^{-}$ ).

While V<sub>O</sub> are among the most common intrinsic defects in ZnO, and are often considered potential sources of EPR signals, their contribution depends strongly on their charge and spin state. In our case, we assigned the g  $\approx$  1.96 resonance to negatively charged zinc vacancies, based on several consistent observations: the resonance matches well with literature values for  $V_{Zn}^-$  [63,66]; its intensity systematically decreases with increasing crystallite size, as supported by our XRD and SEM data (refer to Figs. 4(c) and 3(b) and (c)), which aligns with the known size-dependence of zinc vacancy-related EPR signals. Moreover, oxygen vacancies in ZnO frequently exist in a neutral (V<sub>O</sub><sup>0</sup>) or doubly ionized (V<sub>O</sub><sup>2-</sup>) state under ambient conditions—both of which are EPR silent due to their diamagnetic nature. This suggests that VO defects may still be present in our samples, as is typical for ZnO; they likely remain non-ionized and thus do not contribute to the observed paramagnetic signal. Specifically, ZnO:Mn0 synthesized @ 160 W displays the smallest average crystallite size and rod dimensions, aligning with other studies that show a reduction in V<sub>Zn</sub> - related EPR signal intensity as particle size increases.

The Mn-doped ZnO samples display typical anisotropic sextet hyperfine lines of Mn $^{2+}$ , indicating the incorporation of Mn $^{2+}$  ions in the ZnO lattice. Six hyperfine transitions arise due to the Mn hyperfine coupling with the nuclear spin  $I_{Mn}=5/2$ , wherein the sextets belong to the transitions  $m_{S(Mn)} \longrightarrow m_{S(Mn)}+1$  [11,63]. Along the hyperfine resolved sextet line, zero-field splitting is observable in the Q-band measured EPR spectra, which is observable due to the high MW-frequency (33.89 GHz) at which the EPR measurements were performed [99,63].

Hyperfine lines are visible without substantial broadening (compared to the literature), indicating that Mn ions replace the  $\rm Zn^{2+}$  sites [100]. The following EPR parameters are observable: g-value g=2.0019, hyperfine coupling constant A=220 MHz, zero-field splitting parameters D=720 MHz and E=22 MH, which are in concordance with the already reported literature [101,100,63], which provides proof for the  $\rm Mn^{2+}$  substitution of  $\rm Zn^{2+}$  in the crystal lattice. The samples synthesized with 160 W microwave powers show the highest  $\rm Mn^{2+}$ -related EPR signal, indicating that synthesizing the ZnO structures at this power facilitates the incorporation of more Mn ions into the ZnO lattice.

Cyclic voltammetry is a fundamental electrochemical technique used to understand electrode materials' redox behavior and capacitive properties. In CV testing, the electrode's potential is increased linearly at a specific scan rate, and the resulting current-potential profile provides insights into the kinetics of redox reactions, charge transfer processes, and ion diffusion at the electrode interface [67]. Under CV testing, ZnO exhibits a pseudocapacitive curve rather than behaving as an electrical double-layer capacitor (EDLC). In EDLC, the charge is stored through the physical adsorption of ions at the electrode/electrolyte interface, which appears rectangular in resulting current-voltage graphs [102]. However, ZnO, a transition metal undergoing reversible Faradaic reactions, shows distinct peaks due to its slower and more complex ion diffusion processes compared to the rapid electrostatic storage in EDLC [103]. The redox processes in ZnO are controlled by the kinetics of ion transport that involves Faradaic redox reactions, which imparts a diffusive behavior. The EDLC mechanism involves the rapid physical transportation of ions through the layer between the two electrode materials [104]. The synthesis techniques directly affect the capacitive behavior of the electrode materials. The control of the defect can explain the reason behind this [105]. While ZnO:Mn0 @ 800 W has defects that facilitate ion diffusion, indicated by minor redox peaks, ZnO:Mn0 @ 320 W results in a rectangular-like shape.

Although most of the synthesis techniques mainly have a positive effect on the Faradaic properties of the ZnO, it is possible to say that controlling synthesis parameters and indirectly controlling defect centers result in different electrode behaviors with the same composition. Additionally, doping with elements like Mn can further enhance these Faradaic processes by providing additional active sites and improving electron conductivity [106]. Fig. S-CV\* shows the CV graph of the SC devices tested at five different scan rates (10, 20, 50, 100, and 200 mV/s), while in Fig. 8, the specific capacitance at different scan rates is presented for all undoped and M-doped ZnO samples synthesized at various microwave powers. The four different synthesis microwave powers and the varying dopant levels are expected to yield enhanced reactive surfaces. In other words, undoped ZnO should show prominent redox peaks. For samples synthesized @ 160 W, peaks rise as the dopant level increases. Especially moving from ZnO:Mn2 to ZnO:Mn5, while it preserves the shape, the highest point of the peaks almost doubles. This shows that the dopant effect enhances the pseudocapacitive behavior of ZnO by facilitating ion diffusion.

In ZnO-based systems, EDLC arises from the electrostatic accumulation of ions at the electrode-electrolyte interface without any charge transfer. This behavior is typically associated with nanostructured ZnO materials (nanowires, nanorods, and nanoparticles) that offer a high surface area and porous architecture, facilitating ion adsorption and desorption during cycling [48]. On the other hand, pseudocapacitance in ZnO is attributed to fast and reversible redox reactions involving the Zn $^{2+}$ /Zn redox couple and surface oxygen species. However, bulk ZnO has relatively poor intrinsic conductivity and a limited number of redoxactive sites, which can restrict pseudocapacitive contributions. These limitations are often addressed through strategic doping [107].

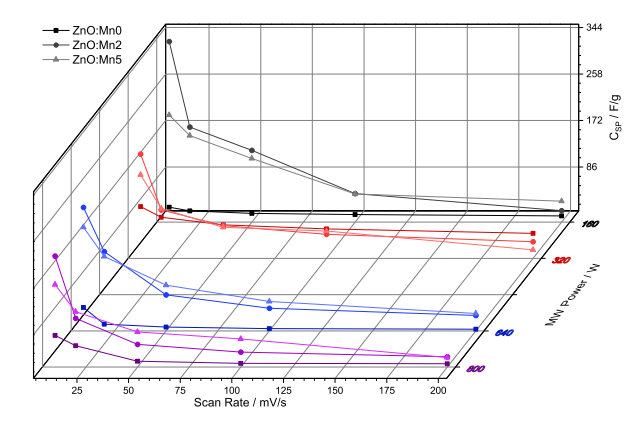


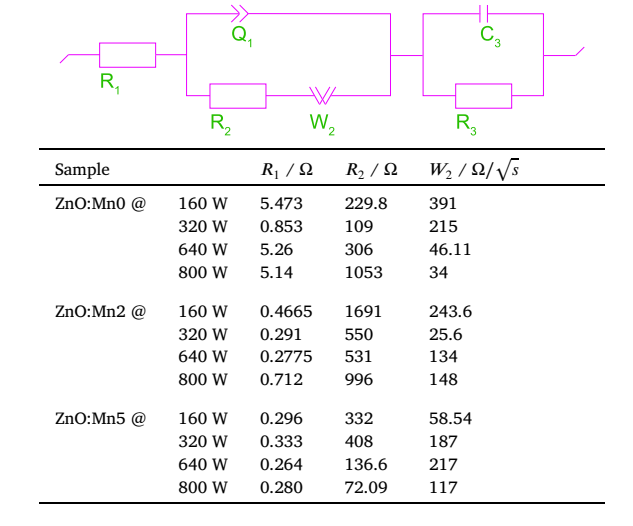
**Fig. 8.** The specific capacitance evolution as a function of the scan rate of undoped and Mn-doped ZnO samples synthesized at different microwave powers.

The most sudden change of the dopant effect can be observed in the 320 W samples. As it is doped with 2% Mn, peaks become more defined, indicating that Mn facilitates redox reactions by creating reactive sites. However, moving towards 5%, the threshold of the optimal reactive sites is being exceeded. It can be understood that peaks have become more defined, but not because there have been more redox reactions; yet, now the resistive effect of ions has appeared and negatively affects the performance by dropping both maximum current values and specific capacitance. ZnO:Mn0 @ 640 W presents a pseudocapacitive behavior with slight peaks of redox reactions. The dopant effect on this sample reveals increased capacitive properties and peaks. On the other hand, the dopant effect occurring in the synthesis of 800 W ZnO is more drastic, indicated by the additional defined peaks in the current potential profile. Although the increasing dopant level negatively affects possible reactive sites, ZnO:Mn2 shows enhanced Faradaic reactions that increase the supercapacitor's diffusive properties and direct performance.

The CV plots are further analyzed to obtain the specific capacitance  $(C_S)$  of the SC devices by evaluating the area enclosed in the CV curves and using the following formula:  $C_S = \frac{A}{2mk\Delta V}$ , where A is the area under the CV curves, m is the mass of electrode material, k is the scan rate, and  $\Delta V$  is the voltage window. The  $C_S$  results are shown in Fig. 8. ZnO:Mn2 samples show the highest specific capacitance, followed by ZnO:Mn5, and ZnO:Mn2. The variation in  $C_S$  value can be attributed to several factors. Mn doping provides additional charge carriers in the structure of ZnO, as evidenced by the EPR results. ZnO:Mn2 concentration balances additional charge carriers and structure integrity. Increasing the dopant concentration in ZnO:Mn5 provides more charge carriers. However, it negatively affects the structure, as shown in the decreased crystallinity in XRD results and the breakage of the nanorods shown in the SEM images.

To further understand the working mechanism of the SC devices and the effect of the Mn dopant, the Dunn technique was applied [108]. The equation is expressed as  $I(V) = k_1 \cdot v + k_2 \cdot \sqrt{v}$ , where  $k_1$  represents the capacitive current,  $k_2$  represents the diffusive current, and v is the scan rate. The relative contributions of each mechanism can be quantified by analyzing the slope and intercept of a Dunn plot. The Dunn technique is used to provide insight into the working mechanism of the SC devices by revealing the contributions of the capacitive mechanism that is associated with the rapid physical transport of ions between the electrodes in the EDLC layer, and between the diffusive mechanism that involves Faradaic redox reactions that further enhances the performance of the devices. The Faradaic redox reactions are often associated with the rapid transfer of ions and electrons [109]. These mechanisms are affected by several factors such as the scan rate and the internal resistance of the electrode materials. The results are shown in Fig. 9. The Dunn technique results reveal an increase in the diffusive contribution for ZnO:Mn2 compared to ZnO:MnO at all microwave powers, except for 800 W, where ZnO:Mn0 shows around 90% diffusive contribution, whereas ZnO:Mn2

**Table 1**Illustration of the equivalent circuit and equivalent circuit components' values obtained from the Z-Fit of the Nyquist plots.



shows 85% diffusive contribution at 10 mV/s scan rate. First, at a lower scan rate of 10 mV/s, there is sufficient time for the electrochemical reactions to occur. Thus, the diffusive mechanism generally increases at lower scan rates compared to higher scan rates, where the capacitive contribution that involves the rapid transport of ions increases. The increase in the diffusive mechanism for ZnO:Mn2 is attributed to the additionally added charge carrier spots in the structure of ZnO that contribute to increasing the effect of the Faradaic reactions @ 160, 320, and 640 W. For ZnO:Mn2 @ 800 W, however, the effect decreases due to the decrease of the aspect ratio as shown in the SEM histograms, which is not sufficient for the electrochemical reactions to take place and contribute to the diffusive mechanism that involves Faradaic redox reactions. Manganese ions, particularly in variable oxidation states such as Mn<sup>2+</sup>, Mn<sup>3+</sup>, and Mn<sup>4+</sup>, bring intrinsic redox activity to the system [57]. When Mn is doped into the ZnO lattice, it introduces redox centers that reversibly undergo electron transfer reactions during charging and discharging. These redox transitions - between Mn<sup>2+</sup>/Mn<sup>3+</sup> and Mn<sup>3+</sup>/Mn<sup>4+</sup> - facilitate faradaic reactions at or near the surface of the electrode material [74]. As a result, charge storage is no longer limited to surface ion adsorption; instead, it involves fast, reversible redox processes within the material's bulk or near-surface regions [72]. Moreover, Mn doping generates oxygen vacancies within the ZnO structure, improving electrical conductivity and providing additional active sites for redox interactions with electrolyte ions [110]. These vacancies serve as entry points or anchoring spots for ions from the electrolyte, further enhancing the depth and speed of redox reactions. Combining these vacancies with Mn's multiple oxidation states results in a higher density of faradaic sites [111].

Electrochemical impedance spectroscopy is a crucial analytical technique for understanding the electrical properties of SC devices. It is a valuable method that provides insights into the charge transport, resistance, capacitance, and interfacial phenomena essential for optimizing material performance. The electrochemical impedance graphs are shown in Fig. S-PEIS\*. All the graphs reveal the presence of multiple charge transfer processes that most likely include an electrode-electrolyte interface, a charge transfer resistance, and a diffusion-controlled process indicated by the presence of the Warburg element straight line [112]. Z-fit was carried out on the impedance data to get further insight into the resistance values of the SC devices, as shown in Fig. S-PEIS\*.

The equivalent circuit and the value of the results of the Z-fit are displayed in Tables 1 and T-PEIS\*. The ZnO:Mn2 samples show the lowest values for the electrolyte-electrode resistance while having the highest

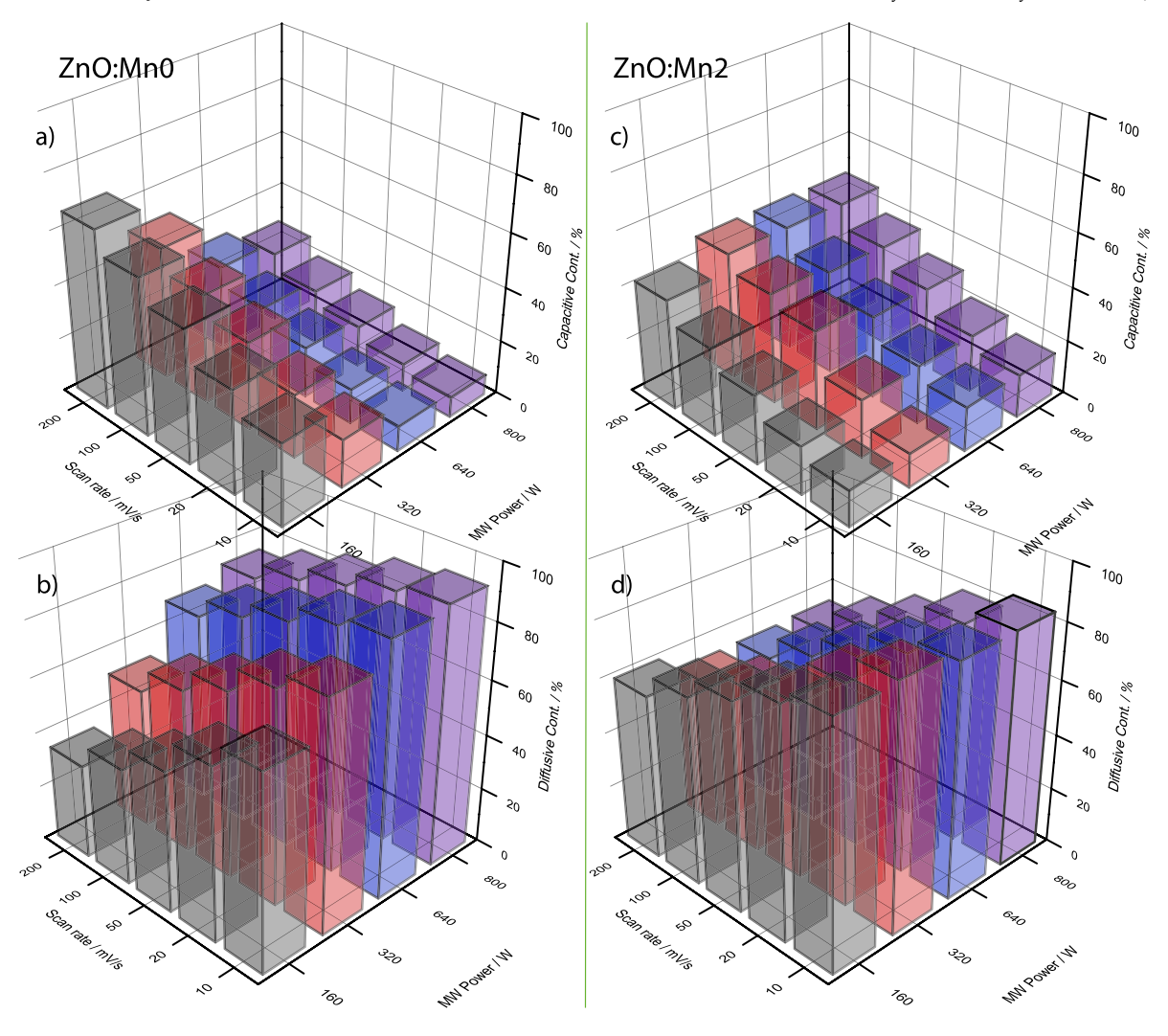


Fig. 9. Capacitive (a) - diffusive (b) contribution of ZnO:Mn0 @ 160 W, and capacitive (c) - diffusive (d) contribution of ZnO:Mn2 @ 160 W obtained employing the Dunn method showing the effect of the dopant element on the charge mechanism.

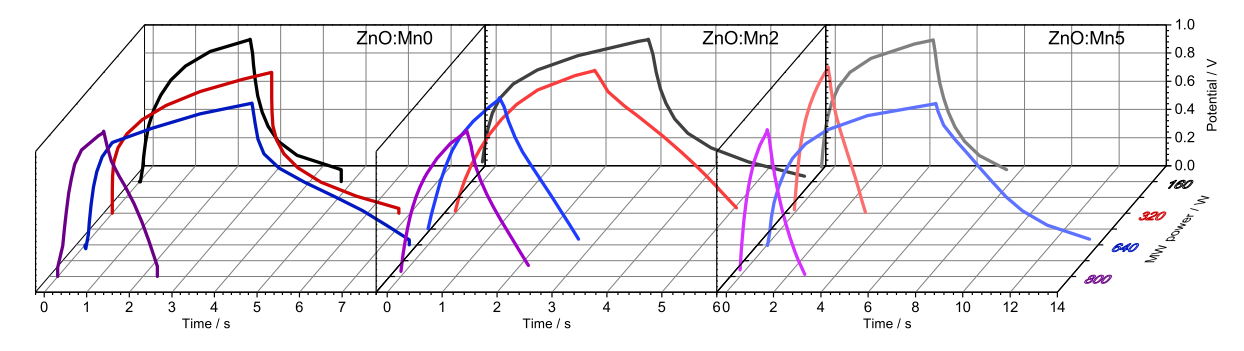
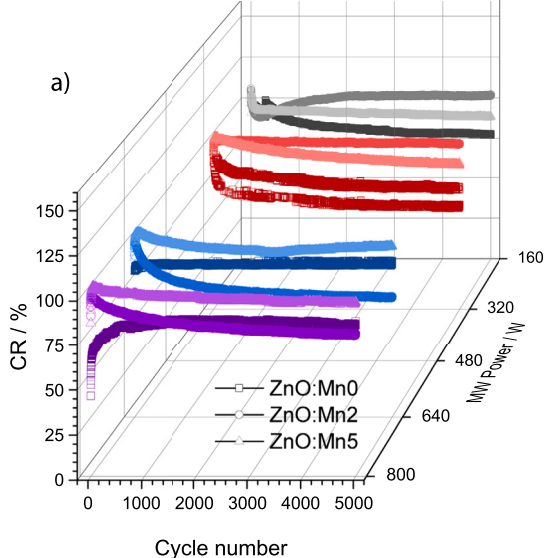


Fig. 10. GCPL plots of undoped and Mn-doped ZnO samples synthesized at different microwave powers highlighting a triangular shape, an indicator of the efficient charge transfer mechanism.

values for the charge transfer resistance. This behavior could be correlated with the interaction between Mn dopant ions and Zn ions in the structure of ZnO. At lower dopant concentrations, Mn ions substitute Zn ions in the structure, as evidenced by the EPR measurements, which disrupts the oxygen vacancies in the structure, thus increasing the charge transfer resistance. This effect is reduced by adding a higher Mn dopant concentration in the system, as shown in the ZnO:Mn5 samples [113,114].

GCPL graphs are instrumental in evaluating the electrochemical performance of materials used in SC devices. Fig. 10 shows the GCPL graphs

of the undoped and Mn-doped samples synthesized with varying microwave powers. ZnO:Mn2 samples generally display a better triangular shape of the GCPL curve, indicating the devices' more efficient charge transfer mechanism [115]. The shape of the GCPL graph can be directly correlated with the working mechanism of the SC device displayed in the Dunn technique's results. The slight deviation from the triangular shape into a semi-triangular shape in ZnO:Mn2 @ 160 W and ZnO:Mn2 @ 320 W samples indicates a more dominant diffusive working mechanism that involves Faradaic redox reactions in addition to the EDLC physical mechanism [116]. This additional contribution of the diffu-



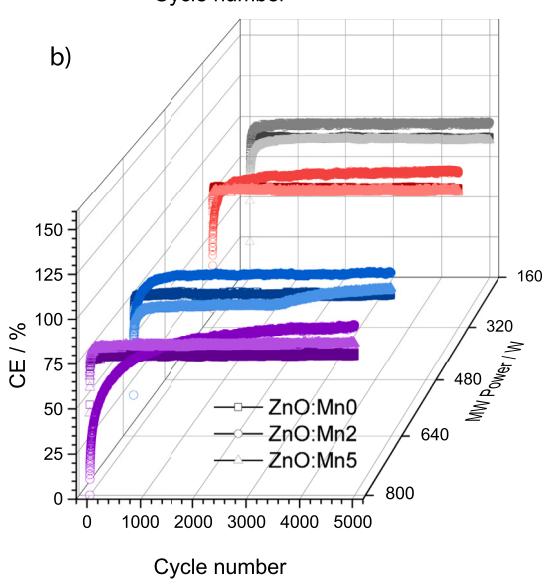


**Fig. 11.** The capacitive retention - CR (a) and Coulombic efficiency - CE (b) of the undoped and Mn-doped ZnO samples synthesized at different microwave powers obtained after 5000 cycles.

sive mechanism seems to positively impact the performance of the SC devices, as it shows an increase in the specific capacitance values for ZnO:Mn2 @ 160 W samples.

In addition to the GCPL profiles, the stability of the SC devices was evaluated over 5000 cycles, as shown in Fig. 11, which displays the capacitive retention and Coulombic efficiency of the undoped and Mndoped ZnO samples. While all samples display adequate stability of over 70%, interestingly, the ZnO:Mn2 samples display higher stability at lower microwave powers of 160 W and 320 W, while ZnO:Mn5 samples, on the other hand, show improved stability at higher microwave powers of 640 W and 800 W. This behavior can be attributed to the role of Mn dopant on the structure and morphology of ZnO. While the 70% stability is considered to be modest in comparison to the values reported in the literature, however, it is important to consider that the ZnO and Mn-doped ZnO nanorods-based systems investigated in our study were synthesized via a low-temperature, scalable microwave-assisted hydrothermal method without any conductive additives or carbon supports. While offering structural simplicity and synthetic ease, these minimalist electrode architectures often exhibit lower cycling durability than composite systems. Similar results of retention have been reported pre-

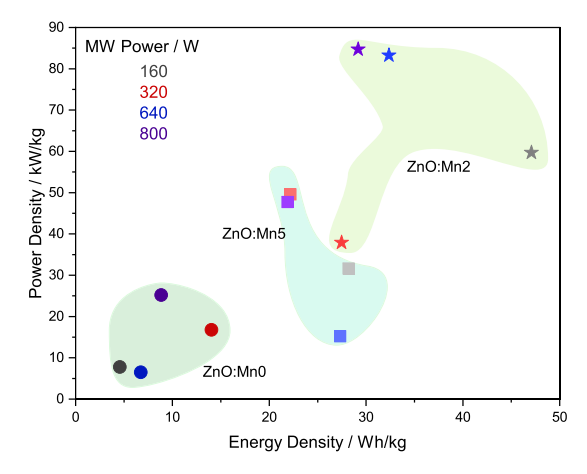


**Fig. 12.** Ragone plot showing the energy and power densities of the symmetric supercapacitor devices based on undoped and Mn-doped ZnO samples synthesized at different microwave powers.

viously. For instance, Hassan et al. [117] reported capacitive retention of 68% after 5000 cycles. Mn dopant is reported to alter the structure of ZnO nanorods into nanoflowers [118]. These results suggest that lower Mn doping levels may favor the formation of stable structures under milder synthesis conditions. In contrast, higher doping levels might require increased energy input to achieve optimal microstructural features that enhance stability. Fig. 11(b) also shows the Coulombic efficiency (CE) of the undoped and Mn-doped ZnO samples. CE measurements are crucial for industrial applicability as they offer insight into the charge reversibility and electrode durability [119]. Mn seems to positively impact the CE of the ZnO samples, increasing the values from around 85 to 95%, reflecting adequate charge-discharge stability and charge transfer reversibility, despite the modest capacitive retention values of the undoped ZnO samples.

Fig. 12 shows the Ragone plot of the SC devices, displaying each device's maximum achieved power density and energy density. The energy density  $(E_D)$  was calculated using the following equation:  $E_D$  $\frac{1}{2}C_S \cdot V^2$ , where  $C_S$  is the specific capacitance and V is the potential window, and the power density  $(P_D)$  was calculated with:  $P_D = \frac{E_D}{\epsilon}$ , where *t* is the discharge time obtained from the GCPL measurements for each device. The ZnO:Mn2-based supercapacitor device outperforms the other devices in energy and power density. The improved performance of ZnO:Mn2 can be attributed to several factors. First, integrating the Mn<sup>2+</sup> ions into the structure of ZnO contributes to adding extra charge carriers, thus improving the aforementioned diffusive mechanism associated with Faradaic redox reactions in the system. ZnO:Mn2 provides a balance between providing sufficient charge carriers without compromising the structure of ZnO, as in the case of ZnO:Mn5, where the excessive integration of Mn2+ led to decreasing the rate of crystallinity and an increase in the crystal cell volume. It is worth mentioning that even amongst the ZnO:Mn2 samples, the performance varies with the use of microwave power during the synthesis process. ZnO:Mn2 @ 620 W and 800 W display higher power density values of 83.2 kW/kg and 84.7 kW/kg, respectively, than ZnO:Mn2 @ 160 W, which shows a power density value of 59.7 kW/kg. However, ZnO:Mn2 @ 160 W shows a higher energy density value of 47.1 Wh/kg than that of ZnO:Mn2 @ 640 W and 800 W, with 32.37 Wh/kg and 29.18 Wh/kg values. The variation of results based on the microwave power used during the synthesis can be better understood by considering the effect of the microwave power on ZnO's crystalline structure and morphology. The power of 160 W provided the highest aspect ratio of ZnO nanorods, which possesses favorable conditions for electrochemical reactions, thus increasing the energy density value of the SC device.

On the other hand, powers of 640 W and 800 W yield more dense nanorods with smaller aspect ratios than 160 W, a condition that fa-

Table 2
Performance comparison of the samples reported herein with other similar systems. Legend: GNR - Graphene nano ribbons, LRGONR - Lacey reduced graphene oxide nano ribbons, CNO - Carbon nano onions, ZnO NR@Ni-Co LDH CNSAs - ZnO nanorods wrapped in ultrathin Ni-Colayered double hydroxide composite nanosheet arrays, AAO - Silver coated anodic aluminum oxide.

E <sub>1</sub>	$\mathbb{E}_2$	$C_S$ / F/g	$P_D$ / kW/kg	$E_D$ / Wh/kg	Ref.
ZnO@GNR	LRGONR	125	1.18	9.4	[120]
CNO-ZnO	Symm	68.5	8.1	10	[121]
ZnO@MnO <sub>2</sub>	AC	907	6.5	17	[122]
ZnO-NR@Ni - Co LDH CNSAs	AC	2683.8	1.11	40.04	[123]
ZnO-NPs@P-Si	Symm	547	-	-	[124]
MnO <sub>2</sub> - AAO	Symm	132	36	26.4	[125]
ZnO:Bi	Symm	177	1.497	55	[126]
NiO:Ce	Symm	122	0.700	8.17	[127]
ZnO:Sr	Symm	698	_	_	[128]
ZnO:Cd - NR	Symm	627	_	_	[129]
CeO <sub>2</sub> :Ni NP	Symm	446	_	_	[130]
ZnO:Ce	Symm	338	-	_	[131]
ZnO:Mn2 @160 W	Symm	340	59.7	47.1	t.w.

vors the rapid transport of ions and thus increases the power density of the SC device. To evaluate our material following similar systems, Table 2 summarizes electrochemical parameters obtained from similar material systems. Combining ZnO with graphene and other carbonbased nanomaterials contributes to the increase of power density due to the high active surface area of carbon-based materials that offer favorable spots for the rapid transportation of ions, increasing both power density and specific capacitance. This increase, however, might negatively affect the energy density values due to suppression of Faradaic redox reactions due to the rapid movement of ions, as shown in the results reported by Sahu et al. [120], Mohapatra et al. [121], Radhamani et al. [122], Liu et al. [123]. When doped with different elements, ZnO shows improved supercapacitive properties, as demonstrated by Angelin et al. [126], where Bi-doped ZnO nanostructures in symmetric supercapacitors showed specific capacitance of 177 F/g at 2 A/g with a great cycle stability of 89.6% capacitance retention after 3000 cycles at 2.8 A/g. When doped with Sr [128] or Cd [129] ions, ZnO had a specific capacitance of 698 F/g at 5 mV/s and of 627 F/g at 1 A/g, respectively, with capacitance retention after 5000 GCD cycles at 1 A/g of 95.4% and 93.3%, but no energy and power density values were reported in both cases.

Hassan et al. [124] successfully obtained ZnO nanoparticles from spent Zn-C batteries through thermal growth on top of porous silicone substrates, and they reported a high specific capacitance value of 547 F/g. While the specific capacitance is high, no information about power and energy densities was reported. The nanoparticle morphology of ZnO might achieve high specific capacitance values. Still, the nanorods' morphology is more favorable for both rapid ion transportation processes and for providing a high active surface area of electrochemical Faradaic redox reactions, thus increasing both the energy density and power density [132,133,48].

This study presents methods to regulate desirable electrochemical characteristics by adjusting the microwave power during synthesis and by varying the concentration of  $\mathrm{Mn}^{2+}$  ions in the ZnO lattice.

#### 4. Conclusions

The study highlights the critical role of Mn ions in improving the supercapacitor performance of ZnO nanorods. The synthesis process is identified as crucial, with Mn-doping effectively optimizing charge carriers and enhancing electrochemical reaction efficiency. The optimal performance is observed in ZnO:Mn2 nanorods synthesized at a microwave power of 160 W, achieving an impressive 59.7 kW/kg power density and 47.1 Wh/kg energy density, exhibiting over 90% stability and maintaining stability over 5000 cycles. The findings suggest that power and microwave conditions significantly influence the structural

and energy properties. The morphology and specific surface area of the ZnO nanorods are directly affected by the Mn dopant concentration and the microwave power used in the synthesis procedure. Increasing the Mn concentration decreases the length and diameter of the nanorods, while increasing the microwave power decreases the specific surface area of the material from 61 m<sup>2</sup>/g at 160 W to 35.5 m<sup>2</sup>/g at 800 W. Photoluminescence measurements proved that with Mn doping the intensity of zinc vacancy-related emissions are reduced, highlighting that Mn ions replace the zinc vacancies. The dopant Mn ions also occupy interstitial positions, changing the oxygen vacancies. Electron paramagnetic resonance spectroscopy results showed a high concentration of monoionized zinc vacancies in the case of the unpode ZnO samples, which are replaced by Mn<sup>2+</sup> ions in the doped samples, while the samples synthesized at 160 W microwave powers show the highest Mn<sup>2+</sup>-related EPR signal, indicating that synthesizing the ZnO structures at this power facilitates the incorporation of more Mn ions into the ZnO lattice.

Mn-doped ZnO nanorods offer improved electrochemical performance for supercapacitors, but several challenges hinder their practical applications. Despite an increase in conductivity, the energy density of the material remains low. Doping ZnO with  $\mathrm{Mn}^{2+}$  ions can lead to increased internal resistance, which reduces charge transfer efficiency. Mechanical stress and structural degradation after numerous chargedischarge cycles also decrease long-term stability. The synthesis process is crucial because variations in microwave power and Mn doping concentrations can lead to defects or aggregation that compromise performance. Therefore, optimizing the synthesis technique by carefully adjusting parameters such as microwave power and Mn doping levels is essential to address these challenges effectively. Moreover, enhancing mechanical durability by hybrid nanostructures or other materials will help to reduce mechanical stress problems. Improving conductivity and general electrochemical performance depends on controlling defect centers, especially concerning oxygen vacancy concentration. Combining these techniques helps Mn-doped ZnO nanorods to be more feasible for practical supercapacitor uses and guaranteeing improved energy storage system performance.

## CRediT authorship contribution statement

Mohamad Hasan Aleinawi: Writing – original draft, Visualization, Methodology, Investigation, Formal analysis, Conceptualization. Ameen Uddin Ammar: Writing – review & editing, Writing – original draft, Investigation, Formal analysis. Duygu Şentürk: Writing – original draft, Visualization, Investigation, Formal analysis. Lucian Barbu-Tudoran: Investigation, Formal analysis. Oluwatosin Johnson Ajala: Writing – original draft, Investigation, Formal analysis. Defne Eşkin: Writing – original draft, Visualization, Investigation, Formal analysis.

**Feray Bakan Misirlioglu:** Writing – review & editing, Writing – original draft, Investigation, Formal analysis. **Arpad Mihai Rostas:** Writing – review & editing, Writing – original draft, Visualization, Validation, Supervision, Investigation, Formal analysis, Conceptualization. **Emre Erdem:** Writing – review & editing, Writing – original draft, Validation, Supervision, Investigation, Conceptualization.

## **Declaration of competing interest**

The authors declare that they have no known competing financial interests or personal relationships that could have appeared to influence the work reported in this paper.

#### Acknowledgements

EE, DE, and DS acknowledge the support of the Sabanci University Program for Undergraduate Research (PURE).

AMR acknowledges the support of a grant from the Ministry of Research, Innovation and Digitization, CNCS—UEFISCDI, project number PN-IV-P2-2.1-TE-2023-0048, within PNCDI IV.

MHA and EE acknowledge the bilateral project, which was initiated as part of the collaboration between the University of Connecticut (UCONN) and Sabanci University (SU).

#### Appendix A. Supplementary material

Supplementary material related to this article can be found online at https://doi.org/10.1016/j.jcis.2025.138012.

#### Data availability

Data will be made available on request.

#### References

- T.T. Hoang, Noble Metal-Manganese Oxide Nanohybrids Based Supercapacitors, Elsevier, 2019.
- [2] D. Su, Z. Tang, J. Xie, Z. Bian, J. Zhang, D. Yang, D. Zhang, J. Wang, Y. Liu, A. Yuan, et al., Co, Mn-LDH nanoneedle arrays grown on Ni foam for high performance supercapacitors, Appl. Surf. Sci. 469 (2019) 487–494.
- [3] M. Cui, X. Meng, Overview of transition metal-based composite materials for supercapacitor electrodes, Nanoscale Adv. 2 (2020) 5516–5528.
- [4] M. Stefan, B. Kocabas, A. Güngör, D. Toloman, A.M. Rostas, R.C. Suciu, S. Macavei, I. Ganea, I. Perhaita, S. Tripon, et al., Manganese-doped zinc oxide recycled from spent alkaline batteries for photocatalysis and supercapacitor applications, J. Energy Storage 99 (2024) 113419.
- [5] S. Kour, S. Tanwar, A. Sharma, A review on challenges to remedies of MnO<sub>2</sub> based transition-metal oxide, hydroxide, and layered double hydroxide composites for supercapacitor applications, Mater. Today Commun. 32 (2022) 104033.
- [6] H.M. Umran, A.A. Alibage, Current research on transition metal oxide materials used to improve super-capacitor performance, AIP Conf. Proc. 3091 (2024) 040005.
- [7] C. Zhao, C. Yu, M. Zhang, H. Huang, S. Li, X. Han, Z. Liu, J. Yang, W. Xiao, J. Liang, et al., Ultrafine MoO<sub>2</sub>-carbon microstructures enable ultralong-life power-type sodium ion storage by enhanced pseudocapacitance, Adv. Energy Mater. 7 (2017) 1602880.
- [8] R. Nasser, X.-L. Wang, J. Tiantian, H. Elhouichet, J.-M. Song, Hydrothermal design of CoMoO<sub>4</sub>@CoWO<sub>4</sub> core-shell heterostructure for flexible all-solid-state asymmetric supercapacitors, J. Energy Storage 51 (2022) 104349.
- [9] R. Nasser, H. Zhou, A.B.G. Trabelsi, F.H. AlKallas, H. Elhouichet, J.-M. Song, Engineering preparation of the nanocomposite containing CoWO<sub>4</sub> nanodots and its high electrochemical activities, J. Energy Storage 68 (2023) 107763.
- [10] D. Zagorac, J. Zagorac, M. Pejić, B. Matović, J.C. Schön, Band gap engineering of newly discovered ZnO/ZnS polytypic nanomaterials, Nanomaterials 12 (2022) 1595.
- [11] B. Yüksel Price, G. Hardal, M. Açıkgöz, S. Repp, E. Erdem, Effects of MnO doping on the electronic properties of zinc oxide: 406 GHz electron paramagnetic resonance spectroscopy and Newman superposition model analysis, J. Appl. Phys. 118 (2015) 175705.
- [12] H. Teisseyre, D. Jarosz, L. Marona, A. Bojarska, V. Ivanov, P. Perlin, T. Czyszanowski, Homoepitaxial ZnO/ZnMgO laser structures and their properties, Phys. Status Solidi A 218 (2021) 2000344.
- [13] X. Zhao, Q. Li, L. Xu, Z. Zhang, Z. Kang, Q. Liao, Y. Zhang, Interface engineering in 1D ZnO-based heterostructures for photoelectrical devices, Adv. Funct. Mater. 32 (2022) 2106887.

- [14] S. Nadupalli, S. Repp, S. Weber, E. Erdem, About defect phenomena in ZnO nanocrystals, Nanoscale 13 (2021) 9160–9171.
- [15] A.R. Jayakrishnan, J.P. da Silva, S. Sathish, K. Kamakshi, K.C. Sekhar, Pyroelectric nanogenerators in energy technology, in: Nanogenerators, CRC Press, 2022, pp. 161–184
- [16] R. Khan, N.U. Rahman, M.F. Hayat, D. Ghernaout, A.A. Salih, G.A. Ashraf, A. Samad, M.A. Mahmood, N. Rahman, M. Sohail, et al., Unveiling cutting-edge developments: architectures and nanostructured materials for application in optoelectronic artificial synapses, Nanoscale 16 (2024) 14589–14620.
- [17] D.K. Sharma, S. Shukla, K.K. Sharma, V. Kumar, A review on ZnO: fundamental properties and applications, Mater. Today Proc. 49 (2022) 3028–3035.
- [18] K. Srikanth, A. Wazeer, P. Mathiyalagan, S. Vidya, K. Rajput, H.S. Kushwaha, Piezoelectric properties of ZnO, in: Nanostructured Zinc Oxide, Elsevier, 2021, pp. 717–736.
- [19] A.U. Ammar, M.H. Aleinawi, M. Stefan, A. Gungor, A. Popa, D. Toloman, K. Maškarić, E. Saritas, L. Barbu-Tudoran, S. Macavei, et al., Lithium-induced defect centers in nanorod-shaped zinc oxide for supercapacitor applications, Electrochim. Acta (2025) 145806.
- [20] M. Stefan, A.M. Rostas, A.U. Ammar, A. Gungor, E. Saritas, D. Toloman, A. Varadi, S. Macavei, L. Barbu-Tudoran, C. Leostean, et al., Cerium enhanced supercapacitive properties of zinc oxide nanoflowers, Energy Fuels 38 (2024) 19088–19099.
- [21] J. Hu, J. Chen, T. Ma, Z. Li, J. Hu, T. Ma, Z. Li, Research advances in ZnO nanomaterials-based UV photode tectors: a review, Nanotechnology 34 (2023) 232002.
- [22] X. Li, X. Liu, Y. Li, D. Gao, L. Cao, Using novel semiconductor features to construct advanced ZnO nanowires-based ultraviolet photodetectors: a brief review, IEEE Access 9 (2021) 11954–11973.
- [23] M. Que, C. Lin, J. Sun, L. Chen, X. Sun, Y. Sun, Progress in ZnO nanosensors, Sensors 21 (2021) 5502.
- [24] M.T. Noman, N. Amor, M. Petru, Synthesis and applications of ZnO nanostructures (ZONSs): a review, Crit. Rev. Solid State Mater. Sci. 47 (2022) 99–141.
- [25] A. Kołodziejczak-Radzimska, T. Jesionowski, Zinc oxide—from synthesis to application: a review, Materials 7 (2014) 2833–2881.
- [26] P.G. Devi, A.S. Velu, Synthesis, structural and optical properties of pure ZnO and Co doped ZnO nanoparticles prepared by the co-precipitation method, J. Theor. Appl. Phys. 10 (2016) 233–240.
- [27] S. Fabbiyola, L.J. Kennedy, U. Aruldoss, M. Bououdina, A. Dakhel, J. JudithVijaya, Synthesis of Co-doped ZnO nanoparticles via co-precipitation: structural, optical and magnetic properties, Powder Technol. 286 (2015) 757–765.
- [28] S. Ghosh, A. Ghosh, S. Pramanik, P.K. Kuiri, R. Sen, S.K. Neogi, Synthesis of ZnO nanoparticles by co-precipitation technique and characterize the structural and optical properties of these nanoparticles, J. Phys. Conf. Ser. 2349 (2022) 012014.
- [29] J. Hasnidawani, H.N. Azlina, H. Norita, N. Bonnia, S. Ratim, E. Ali, Synthesis of ZnO nanostructures using sol-gel method, Proc. Chem. 19 (2016) 211–216.
- [30] M. Kamalasanan, S. Chandra, Sol-gel synthesis of ZnO thin films, Thin Solid Films 288 (1996) 112–115.
- [31] S. Arya, P. Mahajan, S. Mahajan, A. Khosla, R. Datt, V. Gupta, S.-J. Young, S.K. Oruganti, Influence of processing parameters to control morphology and optical properties of sol-gel synthesized ZnO nanoparticles, ECS J. Solid State Sci. Technol. 10 (2021) 023002.
- [32] S. Amirkhanlou, M. Ketabchi, N. Parvin, Nanocrystalline/nanoparticle ZnO synthesized by high energy ball milling process, Mater. Lett. 86 (2012) 122–124.
- [33] S. Wirunchit, P. Gansa, W. Koetniyom, Synthesis of ZnO nanoparticles by ball-milling process for biological applications, Mater. Today Proc. 47 (2021) 3554–3559.
- [34] P. Giri, S. Bhattacharyya, D.K. Singh, R. Kesavamoorthy, B. Panigrahi, K. Nair, Correlation between microstructure and optical properties of ZnO nanoparticles synthesized by ball milling, J. Appl. Phys. 102 (2007).
- [35] P. Georgiou, K. Kolokotronis, J. Simitzis, Synthesis of ZnO nanostructures by hydrothermal method. J. Nanopart. Res. 6 (2009) 157–168.
- [36] W. Liu, S. Wang, J. Wang, B. Zhang, L. Liu, H. Liu, J. Yang, Supercritical hydrother-mal synthesis of nano-zinc oxide: process and mechanism, Ceram. Int. 48 (2022) 22629–22646
- [37] X. Bai, L. Li, H. Liu, L. Tan, T. Liu, X. Meng, Solvothermal synthesis of ZnO nanoparticles and anti-infection application in vivo, ACS Appl. Mater. Interfaces 7 (2015) 1308–1317.
- [38] Y. Mao, Y. Li, Y. Zou, X. Shen, L. Zhu, G. Liao, Solvothermal synthesis and photocatalytic properties of ZnO micro/nanostructures, Ceram. Int. 45 (2019) 1724–1729.
- [39] S. Kunjara Na Ayudhya, P. Tonto, O. Mekasuwandumrong, V. Pavarajarn, P. Praserthdam, Solvothermal synthesis of ZnO with various aspect ratios using organic solvents, Cryst. Growth Des. 6 (2006) 2446–2450.
- [40] J.J. Schneider, R.C. Hoffmann, J. Engstler, A. Klyszcz, E. Erdem, P. Jakes, R.-A. Eichel, L. Pitta-Bauermann, J. Bill, Synthesis, characterization, defect chemistry, and FET properties of microwave-derived nanoscaled zinc oxide, Chem. Mater. 22 (2010) 2203–2212.
- [41] X.-L. Hu, Y.-J. Zhu, S.-W. Wang, Sonochemical and microwave-assisted synthesis of linked single-crystalline ZnO rods, Mater. Chem. Phys. 88 (2004) 421–426.
- [42] G.P. Barreto, G. Morales, M.L.L. Quintanilla, Microwave assisted synthesis of ZnO nanoparticles: effect of precursor reagents, temperature, irradiation time, and additives on nano-ZnO morphology development, J. Mater. 2013 (2013) 478681.

- [43] E. Mohammadi, M. Aliofkhazraei, M. Hasanpoor, M. Chipara, Hierarchical and complex ZnO nanostructures by microwave-assisted synthesis: morphologies, growth mechanism and classification, Crit. Rev. Solid State Mater. Sci. 43 (2018) 475–541
- [44] Y.-C. Chen, S.-L. Lo, Effects of operational conditions of microwave-assisted synthesis on morphology and photocatalytic capability of zinc oxide, Chem. Eng. J. 170 (2011) 411–418.
- [45] T. Iwamura, S.-i. Goto, M. Sakaguchi, Y. Chujo, Synthesis of submicrometer zinc oxide particles and zinc oxide nanowires using microwave irradiation, Chem. Lett. 45 (2016) 508–510.
- [46] Y. Guo, B. Chang, T. Wen, C. Zhao, H. Yin, Y. Zhou, Y. Wang, B. Yang, S. Zhang, One-pot synthesis of graphene/zinc oxide by microwave irradiation with enhanced supercapacitor performance, RSC Adv. 6 (2016) 19394–19403.
- [47] M. Sreejesh, S. Dhanush, F. Rossignol, H. Nagaraja, Microwave assisted synthesis of rGO/ZnO composites for non-enzymatic glucose sensing and supercapacitor applications, Ceram. Int. 43 (2017) 4895–4903.
- [48] D. Toloman, A. Gungor, A. Popa, M. Stefan, S. Macavei, L. Barbu-Tudoran, A. Varadi, I.D. Yildirim, R. Suciu, I. Nesterovschi, et al., Morphological impact on the supercapacitive performance of nanostructured ZnO electrodes, Ceram. Int. 51 (2025) 353–365.
- [49] C.T. Altaf, T.O. Colak, A.M. Rostas, C. Socaci, M.D. Lazar, L.B. Tudoran, M.H. Aleinawi, F.B. Misirlioglu, I.D. Yildirim, E. Erdem, et al., Zinc oxide nanoflake/reduced graphene oxide nanocomposite-based dual-acting electrodes for solar-assisted supercapacitor applications, Energy Adv. 3 (2024) 1965–1976.
- [50] A.B.G. Trabelsi, R. Nasser, F.H. Alkallas, A.F.B. Saqr, B. El-Gammal, J.-M. Song, H. Elhouichet, Tuning the electrochemical properties of ZnO through chromium doping and its suitability for supercapacitor application, J. Energy Storage 87 (2024) 111487
- [51] S. Singal, A. Joshi, A.K. Tomar, V. Sahu, G. Singh, R.K. Sharma, Vacancies and edges: enhancing supercapacitive performance metrics of electrode materials, J. Energy Storage 31 (2020) 101614.
- [52] G. Sahu, A. Balhara, L. Besra, D. Nechiyil, K. Sudarshan, J. Prakash, S.K. Gupta, S. Chatterjee, Defect enriched luminescent mxene-derived TiO<sub>2</sub> for supercapacitors, Inorg. Chem. Commun. 170 (2024) 113462.
- [53] A.U. Ammar, I.D. Yildirim, F. Bakan, E. Erdem, ZnO and MXenes as electrode materials for supercapacitor devices. Beilstein J. Nanotechnol. 12 (2021) 49–57.
- [54] Q.-L. Wu, S.-X. Zhao, L. Yu, X.-X. Zheng, Y.-F. Wang, L.-Q. Yu, C.-W. Nan, G. Cao, Oxygen vacancy-enriched MoO-3-x nanobelts for asymmetric supercapacitors with excellent room/low temperature performance, J. Mater. Chem. A 7 (2019) 13205–13214.
- [55] A.U. Ammar, M. Stan, A. Popa, D. Toloman, S. Macavei, C. Leostean, A. Ciorita, E. Erdem, A.M. Rostas, All-in-one supercapacitor devices based on nanosized Mn<sup>4+</sup>-doped WO<sub>3</sub>, J. Energy Storage 72 (2023) 108599.
- [56] M. Toufani, S. Kasap, A. Tufani, F. Bakan, S. Weber, E. Erdem, Synergy of nano-ZnO and 3D-graphene foam electrodes for asymmetric supercapacitor devices, Nanoscale 12 (2020) 12790–12800.
- [57] Y. Gao, S. Zhang, X. Li, L. Li, L. Bao, N. Zhang, J. Peng, X. Li, Synergistically optimizing electronic structure and reducing ions transport resistance by oxygen functional groups and defects in carbon for superior sodium capture and potassium storage capability, Carbon 181 (2021) 323–334.
- [58] S. Mrabet, N. Ihzaz, M. Alshammari, N. Khlifi, M. Ba, M. Bessadok, I. Mejri, L. El Mir, Structural, optical, and magnetic properties of V-doped ZnO nanoparticles and the onset of ferromagnetic order, J. Alloys Compd. 920 (2022) 165920.
- [59] T. Ruf, S. Repp, J. Urban, R. Thomann, E. Erdem, Competing effects between intrinsic and extrinsic defects in pure and Mn-doped ZnO nanocrystals, J. Nanopart. Res. 18 (2016) 1–11.
- [60] A. Sharma, P. Kumar, Review on structural, magnetic, optical properties of manganese doped zinc oxide nanoparticles, Mater. Today Proc. (2023).
- [61] L. Wehbi, M. Noun, K. Habanjar, R. Awad, Investigation of the structural and the physical properties of ZnO-NiO-Mn<sub>2</sub>O<sub>3</sub> nanocomposites for photocatalytic applications, Appl. Phys. A 129 (2023) 390.
- [62] V. Gurylev, V. Gurylev, Analysis of defects, in: Nanostructured Photocatalyst via Defect Engineering: Basic Knowledge and Recent Advances, 2021, pp. 103–143.
- [63] A.U. Ammar, I.D. Yildirim, M.H. Aleinawi, M. Buldu-Akturk, N.S. Turhan, S. Nadupalli, A.M. Rostas, E. Erdem, Multifrequency epr spectroscopy study of Mn, Fe, and Cu doped nanocrystalline ZnO, Mater. Res. Bull. 160 (2023) 112117.
- [64] S. Kasap, I.I. Kaya, S. Repp, E. Erdem, Superbat: battery-like supercapacitor utilized by graphene foam and zinc oxide (ZnO) electrodes induced by structural defects, Nanoscale Adv. 1 (2019) 2586–2597.
- [65] S. Yildirimcan, K. Ocakoglu, S. Erat, F.M. Emen, S. Repp, E. Erdem, The effect of growing time and Mn concentration on the defect structure of ZnO nanocrystals: X-ray diffraction, infrared and EPR spectroscopy, RSC Adv. 6 (2016) 39511–39521.
- [66] E. Erdem, Microwave power, temperature, atmospheric and light dependence of intrinsic defects in ZnO nanoparticles: a study of electron paramagnetic resonance (epr) spectroscopy, J. Alloys Compd. 605 (2014) 34–44.
- [67] N. Elgrishi, K.J. Rountree, B.D. McCarthy, E.S. Rountree, T.T. Eisenhart, J.L. Dempsey, A practical beginner's guide to cyclic voltammetry, J. Chem. Educ. 95 (2018) 197–206.
- [68] M. Caglar, S. Ilican, Y. Caglar, F. Yakuphanoglu, Electrical conductivity and optical properties of ZnO nanostructured thin film, Appl. Surf. Sci. 255 (2009) 4491–4496.

- [69] Y. Nagaraju, H. Ganesh, S. Veeresha, H. Vijeth, H. Devendrappa, Synthesis of hierarchical ZnO/NiO nanocomposite wurtz hexagonal nanorods via hydrothermal for high-performance symmetric supercapacitor application, J. Energy Storage 56 (2022) 105924
- [70] A.U. Ammar, F. Bakan-Misirlioglu, M.H. Aleinawi, G. Franzo, G.G. Condorelli, F.N.T. Yesilbag, Y.O. Yesilbag, S. Mirabella, E. Erdem, All-in-one supercapacitors with high performance enabled by Mn/Cu doped ZnO and MXene, Mater. Res. Bull. 165 (2023) 112334.
- [71] E. Samuel, B. Joshi, M.-W. Kim, Y.-I. Kim, M.T. Swihart, S.S. Yoon, Hierarchical zeolitic imidazolate framework-derived manganese-doped zinc oxide decorated carbon nanofiber electrodes for high performance flexible supercapacitors, Chem. Eng. J. 371 (2019) 657–665.
- [72] A.R. Rashid, A.G. Abid, S. Manzoor, A. Mera, T.I. Al-Muhimeed, A.A. AlObaid, S.N. Shah, M.N. Ashiq, M. Imran, M. Najam-Ul-Haq, Inductive effect in Mn-doped ZnO nanoribon arrays grown on ni foam: a promising key for boosted capacitive and high specific energy supercapacitors, Ceram. Int. 47 (2021) 28338–28347.
- [73] M.H. Aleinawi, A.U. Ammar, M. Buldu-Akturk, N.S. Turhan, S. Nadupalli, E. Erdem, Spectroscopic probing of Mn-doped ZnO nanowires synthesized via a microwaveassisted route, J. Phys. Chem. C 126 (2022) 4229–4240.
- [74] A. Das, A. Banerjee, A. Tayal, M.S. Ali, R. Layek, S. Karmakar, P. Sinha, P. Kumbhakar, D. Chattopadhyay, S. Bandyopadhyay, Local structure distortion in Mn, Zn doped Cu<sub>2</sub>V<sub>2</sub>O<sub>7</sub>: supercapacitor performance and emergent spin-phonon coupling, Adv. Mater. 37 (2025) 2416644.
- [75] S. Pearton, D. Norton, K. Ip, Y. Heo, T. Steiner, Recent progress in processing and properties of ZnO, Superlattices Microstruct. 34 (2003) 3–32.
- [76] T. Zheng, Y. Hu, S. Yang, Effect of grain size on the electrochemical behavior of pure magnesium anode, J. Magnesium Alloys 5 (2017) 404–411.
- [77] J. Han, P. Mantas, A. Senos, Defect chemistry and electrical characteristics of undoped and Mn-doped ZnO, J. Eur. Ceram. Soc. 22 (2002) 49–59.
- [78] Y. Abdollahi, A. Abdullah, Z. Zainal, N. Yusof, Synthesis and characterization of manganese doped zno nanoparticles, Int. J. Basic Appl. Sci. 11 (2011) 62–69.
- [79] B.D. Biswas, M.D. Purkayastha, E. Tiwari, S. Denrah, M. Sarkar, G.K. Darbha, T.P. Majumder, Study of the photocatalytic activity of Mn-doped zno nanocomposites depending on their morphology and structure with the variation of manganese concentration. Surf. Interf. 23 (2021) 100902.
- [80] Y.-W. Lee, B.-S. Kim, J. Hong, J. Lee, S. Pak, H.-S. Jang, D. Whang, S. Cha, J.I. Sohn, J.M. Kim, A pseudo-capacitive chalcogenide-based electrode with dense 1-dimensional nanoarrays for enhanced energy density in asymmetric supercapacitors, J. Mater. Chem. A 4 (2016) 10084–10090.
- [81] S. Ozkan, N.T. Nguyen, I. Hwang, A. Mazare, P. Schmuki, Highly conducting spaced tio \_2 nanotubes enable defined conformal coating with nanocrystalline nb \_2 o \_5 and high performance supercapacitor applications, arXiv preprint, arXiv:2005. 01603, 2020.
- [82] B. Dole, V. Mote, V. Huse, Y. Purushotham, M. Lande, K. Jadhav, S. Shah, Structural studies of Mn doped ZnO nanoparticles, Curr. Appl. Phys. 11 (2011) 762–766.
- [83] K.P. Sapkota, I. Lee, M.A. Hanif, M.A. Islam, J.R. Hahn, Solar-light-driven efficient ZnO-single-walled carbon nanotube photocatalyst for the degradation of a persistent water pollutant organic dye, Catalysts 9 (2019) 498.
- [84] I. Qasim, M. Mumtaz, K. Nadeem, S.Q. Abbas, Zinc nanoparticles at intercrystallite sites of ( $Cu_{0.5}Tl_{0.5}$ )  $Ba_2Ca_3Cu_4O_{12}-\delta$  superconductor, J. Nanomater. 2016 (2016) 9781790.
- [85] M. Wang, L. Jiang, E.J. Kim, S.H. Hahn, Electronic structure and optical properties of Zn(OH)<sub>2</sub>:LDA<sup>+</sup> U calculations and intense yellow luminescence, RSC Adv. 5 (2015) 87496–87503.
- [86] C.-C. Tseng, Y.-H. Chou, C.-M. Liu, Y.-M. Liu, M.-D. Ger, Y.-Y. Shu, Microwaveassisted hydrothermal synthesis of zinc oxide particles starting from chloride precursor, Mater. Res. Bull. 47 (2012) 96–100.
- [87] V. Mote, Y. Purushotham, B. Dole, Structural, morphological, physical and dielectric properties of Mn doped ZnO nanocrystals synthesized by sol-gel method, Mater. Des. 96 (2016) 99–105.
- [88] E.N.A.A. Armah, M. Egblewogbe, H.A. Koffi, A.A. Yankson, F.K. Ampong, F. Boakye, J.K.A. Amuzu, R.K. Nkum, Solubility of Mn in ZnO crystallites synthesized using solid state techniques, Adv. Nano Res. 3 (2020) 28–39.
- [89] E. Ercay, S. Ersoy, M. Ozcan, F.B. Misirlioglu, A. Gungor, A. Ozarowski, F. Kaya, A.M. Rostas, C. Kaya, E. Erdem, Enhancing ZnO-based supercapacitors through carbon-induced defect centers, Mater. Res. Soc. Bull. (2025) 1–13.
- [90] T.O. Colak, C.T. Altaf, F.N.T. Yesilbag, Y.O. Yesilbag, I.D. Yildirim, E. Erdem, F.B. Misirlioglu, N.D. Sankir, M. Sankir, Photo-supercapacitors based on zinc oxide/MX-ene paper dual acting electrodes, J. Energy Storage 86 (2024) 111274.
- [91] C.T. Altaf, T.O. Colak, E. Erdem, U. Unal, F.B. Misirlioglu, G.G. Condorelli, N.D. Sankir, M. Sankir, Disulfonated polyarylene ether sulfone membrane for graphitic carbon nitride/zinc oxide based photo-supercapacitors, Electrochim. Acta 456 (2023) 142415.
- [92] T. Zhang, H. Yue, H. Qiu, K. Zhu, L. Zhang, Y. Wei, F. Du, G. Chen, D. Zhang, Synthesis of graphene-wrapped ZnMn<sub>2</sub>O<sub>4</sub> hollow microspheres as high performance anode materials for lithium ion batteries, RSC Adv. 5 (2015) 99107–99114.
- [93] N.S. Norberg, K.R. Kittilstved, J.E. Amonette, R.K. Kukkadapu, D.A. Schwartz, D.R. Gamelin, Synthesis of colloidal Mn<sup>2+</sup>:ZnO quantum dots and high-TC ferromagnetic nanocrystalline thin films, J. Am. Chem. Soc. 126 (2004) 9387–9398.

- [94] H. Kaftelen, K. Ocakoglu, R. Thomann, S. Tu, S. Weber, E. Erdem, EPR and photoluminescence spectroscopy studies on the defect structure of ZnO nanocrystals, Phys. Rev. B, Condens. Matter Mater. Phys. 86 (2012) 014113.
- [95] E. Erdem, Defect induced p-type conductivity in zinc oxide at high temperature: electron paramagnetic resonance spectroscopy, Nanoscale 9 (2017) 10983–10986.
- [96] S. Parashar, B. Murty, S. Repp, S. Weber, E. Erdem, Investigation of intrinsic defects in core-shell structured ZnO nanocrystals, J. Appl. Phys. 111 (2012) 113712.
- [97] A. Janotti, C.G. Van de Walle, Oxygen vacancies in ZnO, Appl. Phys. Lett. 87 (2005) 122102.
- [98] A. Janotti, C.G. Van de Walle, New insights into the role of native point defects in ZnO, J. Cryst. Growth 287 (2006) 58–65.
- [99] S. Misra, Interpretation of Mn<sup>2+</sup> EPR spectra in disordered materials, Appl. Magn. Reson. 10 (1996) 193–216.
- [100] M. Lorenz, R. Böttcher, S. Friedländer, A. Pöppl, D. Spemann, M. Grundmann, Local lattice distortions in oxygen deficient Mn-doped ZnO thin films, probed by electron paramagnetic resonance, J. Mater. Chem. C 2 (2014) 4947–4956.
- [101] A. Ankiewicz, M. Carmo, N. Sobolev, W. Gehlhoff, E. Kaidashev, A. Rahm, M. Lorenz, M. Grundmann, Electron paramagnetic resonance in transition metal-doped ZnO nanowires, J. Appl. Phys. 101 (2007) 024324.
- [102] Y. Gogotsi, R.M. Penner, Energy storage in nanomaterials—capacitive, pseudocapacitive, or battery-like?, 2018.
- [103] P. Bhojane, Recent advances and fundamentals of pseudocapacitors: materials, mechanism, and its understanding, J. Energy Storage 45 (2022) 103654.
- [104] C. Zhang, D. He, J. Ma, W. Tang, T.D. Waite, Faradaic reactions in capacitive deionization (CDI)-problems and possibilities: a review, Water Res. 128 (2018) 314–330.
- [105] S. Najib, F. Bakan, N. Abdullayeva, R. Bahariqushchi, S. Kasap, G. Franzò, M. Sankir, N.D. Sankir, S. Mirabella, E. Erdem, Tailoring morphology to control defect structures in ZnO electrodes for high-performance supercapacitor devices, Nanoscale 12 (2020) 16162–16172.
- [106] A. Mishra, D. Das, Investigation on Fe-doped ZnO nanostructures prepared by a chemical route, Mater. Sci. Eng. B 171 (2010) 5–10.
- [107] A. Levent, C. Saka, Enhanced electrochemical performance of Zno@sulphur-doped carbon particles for use in supercapacitors. J. Energy Storage 78 (2024) 110120.
- [108] R. Raavi, S. Archana, P.A. Reddy, P. Elumalai, Performances of dual carbon multiion supercapacitors in aqueous and non-aqueous electrolytes, Energy Adv. 2 (2023) 385–397
- [109] S. Gowri, S. Rajkumar, S. Dhineshkumar, J. Aarthi, M. Karthikeyan, A. Ravikumar, J. Princy Merlin, Construction of CuV<sub>2</sub>O<sub>6</sub>-nanostructured electrode material for supercapacitors, MRS Commun. 13 (2023) 460–465.
- [110] A. Das, D. Liu, R.R. Wary, A.S. Vasenko, O.V. Prezhdo, R.G. Nair, Mn-modified ZnO nanoflakes for optimal photoelectrochemical performance under visible light: experimental design and theoretical rationalization, J. Phys. Chem. Lett. 14 (2023) 9604–9611.
- [111] G.R. Dillip, A.N. Banerjee, V.C. Anitha, B. Deva Prasad Raju, S.W. Joo, B.K. Min, Oxygen vacancy-induced structural, optical, and enhanced supercapacitive performance of zinc oxide anchored graphitic carbon nanofiber hybrid electrodes, ACS Appl. Mater. Interfaces 8 (2016) 5025–5039.
- [112] A.C. Lazanas, M.I. Prodromidis, Electrochemical impedance spectroscopy a tutorial, ACS Meas. Sci. Au 3 (2023) 162–193.
- [113] W. Oo, L.V. Saraf, M.H. Engelhard, V. Shutthanandan, L. Bergman, J. Huso, M.D. Mccluskey, Suppression of conductivity in Mn-doped ZnO thin films, J. Appl. Phys. 105 (2009).
- [114] T. Oshio, K. Masuko, A. Ashida, T. Yoshimura, N. Fujimura, Effect of Mn doping on the electric and dielectric properties of ZnO epitaxial films, J. Appl. Phys. 103 (2008).
- [115] D. Anbuselvan, G. Anitha, S. Nilavazhagan, L.B. Chandrasekar, M. Karunakaran, K. Sakthipandi, Electrochemical investigations of Mn-doped ZnO/rGO nanoparticles

- electrode material for supercapacitor application and its enhanced antimicrobial activity. Eur. Phys. J. Plus 139 (2024) 1–16.
- [116] H. Yang, Effects of supercapacitor physics on its charge capacity, IEEE Trans. Power Electron. 34 (2018) 646–658.
- [117] K. Hassan, R. Hossain, V. Sahajwalla, Recycled zno-fused macroporous 3D graphene oxide aerogel composites for high-performance asymmetric supercapacitors, J. Am. Ceram. Soc. 105 (2022) 7467–7478.
- [118] S. Jangu, S. Kumar, K.N. Deepika, C. Jacob, D. Pradhan, Effect of microwave power and Cu doping on MnO<sub>2</sub> nanostructures and its supercapacitor performance, ACS Appl. Electron. Mater. 5 (2023) 3078–3092.
- [119] R. Nasser, H. Zhou, H. Elhouichet, S. Melhi, Z. Li, J.-M. Song, NiFe<sub>2</sub>O<sub>4</sub>@NiCo<sub>2</sub>O<sub>4</sub> hollow algae-like microspheres enabled by Mott-Schottky for electrochemical energy storage, Chem. Eng. J. 489 (2024) 151554.
- [120] V. Sahu, S. Goel, R.K. Sharma, G. Singh, Zinc oxide nanoring embedded lacey graphene nanoribbons in symmetric/asymmetric electrochemical capacitive energy storage, Nanoscale 7 (2015) 20642–20651.
- [121] D. Mohapatra, S. Parida, S. Badrayyana, B.K. Singh, High performance flexible asymmetric CNO-ZnO//ZnO supercapacitor with an operating voltage of 1.8 V in aqueous medium, Appl. Mater. Today 7 (2017) 212–221.
- [122] A. Radhamani, K. Shareef, M.R. Rao, ZnO@MnO<sub>2</sub> core-shell nanofiber cathodes for high performance asymmetric supercapacitors, ACS Appl. Mater. Interfaces 8 (2016) 30531–30542.
- [123] X. Liu, H. Liu, X. Sun, Aligned ZnO nanorod@ Ni-Co layered double hydroxide composite nanosheet arrays with a core-shell structure as high-performance supercapacitor electrode materials, CrystEngComm 22 (2020) 1593–1601.
- [124] K. Hassan, R. Farzana, V. Sahajwalla, In-situ fabrication of ZnO thin film electrode using spent Zn-C battery and its electrochemical performance for supercapacitance, SN Appl. Sci. 1 (2019) 302.
- [125] A. Kumar, A. Sanger, A. Kumar, Y.K. Mishra, R. Chandra, Performance of high energy density symmetric supercapacitor based on sputtered MnO<sub>2</sub> nanorods, ChemistrySelect 1 (2016) 3885–3891.
- [126] M.D. Angelin, S. Rajkumar, A. Ravichandran, M.M. Alam, A.G. Al-Sehemi, Optimization of Bi-doped ZnO nanostructures as highly efficient electrode material for symmetric supercapacitor applications. J. Ind. Eng. Chem. 147 (2024) 436–447.
- [127] J. Alex, S. Rajkumar, S.R. Ali, J. Kunjumon, J.P. Merlin, A. Aravind, D. Sajan, C. Praveen, Charge storage mechanism and pseudocapacitance performance of NiO and Ce-doped NiO synthesized via modified combustion technique, Ceram. Int. 50 (2024) 47317–47332.
- [128] M.D. Angelin, S. Rajkumar, S. Dhineshkumar, A. Ravichandran, A. Ravikumar, J.P. Merlin, One-step facile synthesis of Sr-doped ZnO as electrode material for supercapacitors, J. Mater. Sci., Mater. Electron. 34 (2023) 1107.
- [129] M.D. Angelin, S. Rajkumar, A. Ravichandran, J.P. Merlin, Systematic investigation on the electrochemical performance of Cd-doped ZnO as electrode material for energy storage devices, J. Phys. Chem. Solids 161 (2022) 110486.
- [130] J. Alex, S. Rajkumar, J. PrincyMerlin, A. Aravind, D. Sajan, C. Praveen, Single step auto-igniting combustion technique grown  ${\rm CeO_2}$  and Ni-doped  ${\rm CeO_2}$  nanostructures for multifunctional applications, J. Alloys Compd. 882 (2021) 160409.
- [131] M. Karthikeyan, S. Rajkumar, M. Priyadharshan, Green synthesis of Ce doped ZnO nanoparticles using phyllanthus emblica seed extract for the efficient highperformance supercapacitor application, J. Ind. Eng. Chem. 147 (2024) 608–618.
- [132] S. Di, L. Gong, B. Zhou, Precipitated synthesis of Al<sub>2</sub>O<sub>3</sub>-ZnO nanorod for high-performance symmetrical supercapacitors, Mater. Chem. Phys. 253 (2020) 123289.
- [133] C.T. Altaf, O. Coskun, A. Kumtepe, A.M. Rostas, I. Iatsunskyi, E. Coy, E. Erdem, M. Sankir, N.D. Sankir, Photo-supercapacitors based on nanoscaled ZnO, Sci. Rep. 12 (2022) 11487.